Developing EPR Spectroscopy with ^{15}N@C$_{60}$ to Provide a Basis for Technological Solutions for a Chip-Scale Atomic Clock

Andrew Smalley

Lancaster University

Department of Physics

Abstract

The requirement for highly accurate timekeeping is increasing as technology develops in the spheres of navigation, geolocation, internet communications and financial transactions. Currently, these activities rely on a globally synchronised coordinated time which is kept precise by signals from large, laboratory based atomic clocks. However, these signals can be corrupted or jammed, and in a geopolitically uncertain environment, a reliable local alternative is required. Chip scale atomic clocks provide a portable solution, but currently available devices rely on complex vapour and laser-based technologies which are expensive, consume relatively large amounts of power and have reliability issues in microfabricated form. A chip scale device based on radio frequency EPR with endohedral fullerenes could solve complexity, cost and reliability issues provided it did not sacrifice accuracy. The work in this thesis builds upon previous experimental results, demonstrating some of the improvements required to establish the technological basis for such a clock. An improvement in resonator quality factor is shown to yield a five-fold improvement in signal to noise ratio, with which the clock transition signal of $^{15}N@C_{60}$ is acquired more clearly than was previously possible. The low and zero field transitions of $^{15}N@C_{60}$ are successfully mapped, yielding a precise value for the hyperfine constant and demonstrating the potential of a single resonator to respond to multiple frequencies. This offers reduced complexity for future microfabrication and provides a proof of concept for a method of field stabilisation. These results are discussed in the context of a functional clock and suggestions made for future work toward its realisation.

Table of Contents

List of Tables

List of Figures

24. Transition frequencies at either side of zero magnetic field.
25. The Mu-metal cage into which the spectrometer apparatus was placed to enable low field transition mapping.
26. Low and zero field transitions of $^{15}N@C_{60}$.
27. Low field spectra showing individual sweeps with fits to the resonances.
28. Two sweeps undertaken separately demonstrating coordination in the resonance peaks at a single value in field.
29. Two sweeps at different frequencies, both showing resonances which should only appear on the other.
30. Oscilloscope trace showing modulation of the post-mixed RF1 signal by the amplitude modulation of the output from RF2.
31. Sweeps of each frequency with separate circuits for each and with two coupling loops coaxially adjacent.

Acknowledgements

There are many people who have helped me on my journey to this point, but first and foremost, my heartfelt thanks and utmost gratitude go to my wife, Rebecca. I've arrived at this point from a somewhat unconventional trajectory. After 20 years working in business, with a good, stable career, there was no compelling reason for me to undertake an MSc other than that it is what I wanted to do. I have sacrificed a significant amount of financial security and even lived in a campervan during the week to make this possible. Not only has Rebecca patiently tolerated the impact of this on both of us, she has unequivocally supported me in the adventure and been steadfastly by my side the whole way. Words cannot express how grateful I am for such a wonderful partner in life.

My thanks and gratitude also go to Prof Edward Laird, whose absolute commitment to precision and clarity have undoubtedly made me a better physicist. This, along with his support and trust in allowing me to pursue the research work in my own way, whilst always providing guidance when necessary, have made the last year fascinating, joyful and full of learning and growth. Edward's honesty and integrity are also a beacon of how to conduct science in an ethical and transparent way, and this is something which I feel will guide me for the rest of my career.

Thanks also to Matthew Green and Dr Ed Riordan, who have freely given their time on many occasions to help me with things I didn't understand and to support me through the many moments of frowning and head-scratching that form a large portion of experimental research. And thanks to Eve Clulow, master's project compadre on the team, for many conversations discussing ideas which frequently led to solutions to problems, and for many a disturbing conversation about gyromagnetic ratios.

Special thanks must go to Lucy Wilson in the electronics workshop for soldering about 8 million resonators, particularly after I immediately broke them the first time around!

Finally, my thanks to the people, too numerous to mention all by name, who form the academics and students of the ULT physics department at Lancaster University. As a consultant in organisational dynamics for some time, I know a good working environment when I see one, and this is one of the best I've ever experienced. Whenever anyone has a problem or needs something, there is always someone to help, and the help is always given freely and gladly. To have this level of mutual support without compromising commitment to excellence and self-development is rare, and it has been a very happy and reassuring thing to be a part of.

And finally, finally, my thanks to my dad and my brother, Gavin, for the endless hours in the workshop that gave me a technical foundation and skills as a child which continue to help me find ways to make things work now, even though the things have grown significantly in complexity! And to my mum, whose example of commitment and dedication to a work of passion was second to none, and who wanted to be a physicist before responding to her calling in life. I dedicate this thesis to you.

Declaration

I declare that the work presented in this thesis is, to the best of my knowledge and belief, my own original work. The material has not previously been submitted at any university or for publication, either in its entirety or in part. This thesis does not exceed the maximum permitted word count of 35,000 (excluding the material preceding section 1 and following section 5). The approximate word count of sections 1 to 5 inclusive is 19300.

Andrew Smalley

1. Introduction

1.1 Clocks and Timekeeping

Since the beginning of modern civilisation, accurate timekeeping, and an agreed upon chronology, have been a key cornerstone in the development of complex human society. The agreement of time among people is now global and is formulated using Coordinated Universal Time (UTC) [1]. Most important human activities depend on this to some degree, and the function of almost all advanced technology depends entirely upon its accuracy. Global communication, global navigation satellite systems (GNSS), the World Wide Web and financial markets [2] are examples of technological solutions which require precise, accurate and universally agreed timekeeping.

However, the calculation of a precise timescale and associated base unit, is extremely difficult and is subject to a large number of sources of error, some of which are not obvious. For example, General Relativity is required in order to ensure accurate navigation using satellites (GPS, GLONASS, Galileo) [3], and a recent study [4] demonstrated that anthropogenic climate change will cause a delay in a required future discontinuity adjustment to UTC, due to its effect in reducing the angular velocity of Earth's rotation on its axis.

An early solution to the problem of accurate timekeeping, and one which represents the most prevalent methodology throughout history, is to reference an oscillator whose frequency has some determinable regularity. The oscillations of such can then be counted in order to arrive at a meaningful interpretation of the passage of time.

The earliest and most obvious example of relevant oscillations is the passage of periods of light and dark on Earth, resultant from the planet's axial rotation. Sundials and similar objects have been used since 1500 B.C., or earlier [5], to break up these periods into useful segments by using the light emitted from the Sun to cast a shadow. As the Sun's position changes relative to the instrument, the shadow moves across a plate with delineated sections, providing a natural counting mechanism.

However, such a method has obvious drawbacks for coordinating time, such as seasonal and geographical variations in the length of daylight and the lack of ability to tell the time during periods of darkness. Even following the development of more accurate timekeeping methods, coordination between local solar times caused problems until the 1880s when Greenwich Mean Time was adopted as a national time standard in the UK, and as the international reference for all global time zones [6].

Early attempts to resolve some of the drawbacks of solar-reliant timekeeping involved using flows or reactions of materials whose rates were known or could be controlled. Examples of such things include hourglasses (sand-timers), burning candles and water clocks [6, 7]. However, these solutions all involved relatively short-term duration of function and required regular human intervention to maintain or replenish their resource.

A mechanical oscillator which could operate for a significant duration whilst maintaining a high degree of accuracy was clearly required. An early attempt, which was adopted for several hundred years, was arrived at in Europe in the early 13th century. This involved use of the verge and foliot escapement mechanism [7]. In this arrangement, the verge (a shaft

providing rotation) served as the oscillator, whilst the foliot (a crossbar) included moveable weights, allowing tuning of its moment of inertia and thus control of the oscillatory period of the attached mechanism. Such setups were used in tower clocks across Europe, including in St. Paul's Cathedral in London in 1286 C.E. [7].

Despite the relative technological advance provided by this invention, it was not until the invention of the pendulum clock in the 17th century that the modern concept of truly accurate timekeeping began to become a reality. This arises from the fact that the oscillations of pendula rely solely on two factors which can be precisely known - the length, l, of the pendulum and the acceleration due to gravity, g, on Earth [6, 7].

The oscillations of an ideal pendulum (neglecting damping effects and driving forces) can be described by the equation for simple harmonic motion, with the period of oscillation given by $T = 2\pi\sqrt{\frac{l}{g}}$. [8]. Whilst a real pendulum in a clock is not ideal, using the small angle approximation, its period can still be thus expressed. This constancy and simplicity gave the pendulum an enormous advantage, but its relative vulnerability to disturbances, was still a problem.

Various spring based oscillator designs for watches improved upon the simple pendulum, but the next revolution in timekeeping was built and demonstrated by researchers at Bell Telephone Laboratories. Originally intended as a device to develop frequency and wavelength standards, they produced the first quartz clock, in 1927 [6, 9]. Due to the piezoelectric property of quartz, whereby its crystalline structure deforms in a precise way in response to an applied electric field, small pieces of quartz can be made to resonate by the periodic application of an electrical potential difference at the correct frequency, known as the resonant frequency.

Such quartz pieces typically resonate at tens of thousands of Hz, but the precise frequency is dependent on size and temperature [6]. The quartz forks used in modern timekeeping applications are usually tuned so that their resonant frequency is 32768 Hz, or 2^{15} Hz, which can easily be processed down to the 1 pulse per second required for a clock [10].

This technology is still used in very many applications, including portable devices, to this day, with its reliability and robustness providing advantage over mechanical devices. However, the long term accuracy of even the best quartz controlled mechanisms is below that which is required for modern high precision applications. Additionally, prior to 1967, the calibration of quartz mechanisms to the standard SI second was problematic due to the fact that the second was defined as 1/86400 of the mean solar day [6]. As mentioned above, the solar day is a somewhat unpredictably changeable quantity. The solution to both of these problems is the most recent timekeeping revolution, the atomic clock.

1.2 Atomic Clocks

Atomic Clocks are able to exploit the fact that, in quantum mechanics, all allowed energy levels of relevant systems are quantised, hence, only specific transitions between particular energy levels can occur, resulting in the absorption or emission of a specific amount of energy.

Using the Planck relation, $E = hf$, it is possible to stimulate atoms in a known state to transition to a higher energy state by using precisely controlled electromagnetic illumination. When the frequency of this stimulus, multiplied by Planck's constant, h, is coincident with the energy required to cause the transition, stimulus of the transition occurs and is called a resonance. The frequency itself is referred to as the resonant frequency for the transition. Atomic clocks function using this resonance effect.

These stimulated transitions are not subject to friction or drag, and are hence stable to an extremely high level of precision. This makes atomic clocks many orders of magnitude more precise than their horological predecessors. The proposed endohedral fullerene clock, to which the work of this thesis relates, will function using this modality.
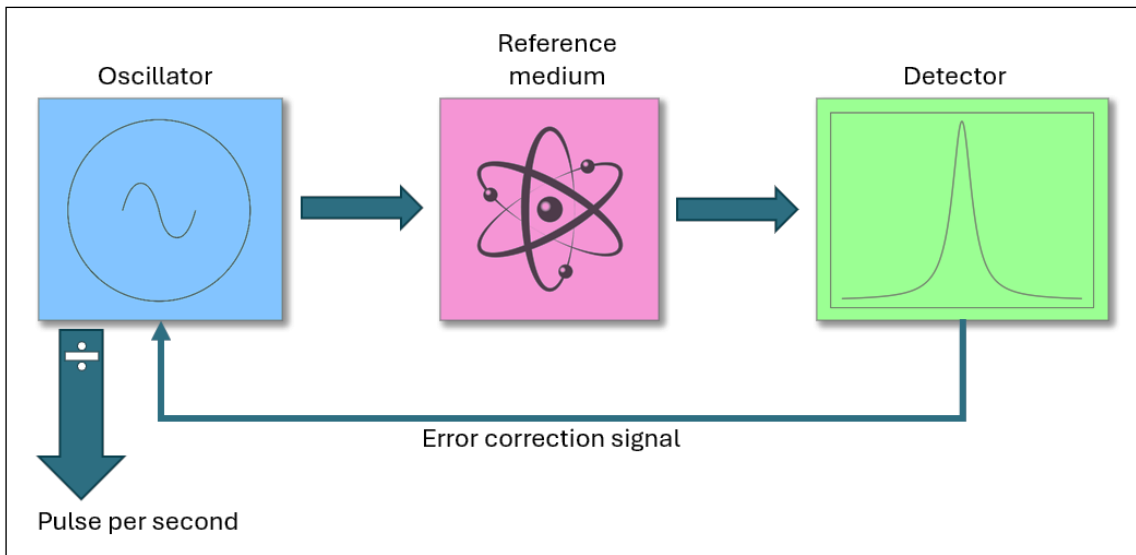
Figure 1. Atomic clock functional schematic. Recreated/adapted from [11]

The overall function of an atomic clock is shown in Figure 1. A local oscillator, LO, produces a frequency which will stimulate a transition in a reference medium. The medium is prepared such that a maximum number of atoms are in the required initial energy state. It is then exposed to the frequency of radiation from the LO before being passed through a detection device which measures the rate of absorption by detecting the proportion of atoms now in the excited state. Maximal absorption indicates that the LO's frequency is correctly calibrated, whilst less than maximal absorption indicates that the frequency has drifted. In this case, an error correction signal is sent to the LO to increase or decrease the frequency accordingly. Simultaneously, a pulse per second output is obtained from the LO by counting the oscillations in the signal and dividing down.

An example of such a system is the thermal Caesium Clock, or Caesium Beam Tube (CBT) Clock, the first working prototype of which was created in 1955 at the National Physical Laboratory (NPL) in the UK [6, 12]. In this system, ^{133}Cs atoms are stimulated into the transition $|3,0\rangle \rightarrow |4,0\rangle$, in the $|F, m_F\rangle$ basis [12]. The atoms are initially heated to approximately 100°C and pass through a spatially varying magnetic field. This removes atoms which aren't in the required ground state, and allows the selected ground state atoms to proceed into a microwave cavity, where they are bombarded with microwaves produced by a quartz-driven oscillator. The atoms leave the cavity through a second magnetic field, which sends only atoms in the excited state through to a detector. This

measures absorption and sends a signal to continually tune the quartz oscillator in order to maximise the rate of absorption [12].

This frequency is in fact how the second is currently defined in SI units – the unperturbed ground state hyperfine transition frequency of Caesium 133; 9 192 631 770 Hz [13]. This ability to measure and define time to a much greater degree of accuracy led to the creation of a new standard, International Atomic Time (TAI) [14], which measures the passage of proper time [15] at Earth's surface to a certainty (a combination of systematic uncertainty, instability and reproducibility) in the order of 10^{-16} [14]. This is achieved by taking a weighted mean of the outputs of around 450 atomic clocks worldwide. Whilst UTC now utilises the SI second, TAI differs from UTC by a varying number of leap seconds, which must be discontinuously inserted into the latter in order to retain its synchronicity with Earth's rotation [16].

Since the invention of the original CBT clock, technology has developed to produce more stable and efficient devices, including caesium fountain clocks and optical frequency standards, which are approaching a certainty of order 10^{-18}, leading to a current discussion regarding further revision of the SI definition of the second [17].

Among the currently used caesium clocks, the caesium fountain clock is considered to be the most stable, and is now used as the primary frequency reference at NPL [18], and NIST [20]. In this design, caesium atoms are laser cooled to around $2\mu K$ using a set of 3 or 6 lasers arranged on mutually orthogonal axes. The cooled atoms are launched upward and descend under gravity, passing through the microwave interrogation cavity (located on their trajectory) twice. This allows for a long interrogation time, lower systematic error, and reduces the temperature sensitivity of the device, allowing more accurate measurement [19].

Both CBT and caesium fountain clocks rely on microwave frequencies to provide the resonance effect. Two further types of production atomic clocks in common usage also use this frequency range: hydrogen masers and rubidium clocks [21]. Hydrogen masers operate by capturing state-selected hydrogen atoms in a storage bulb inside a microwave cavity. These atoms are in the upper hyperfine ground state, the relaxation of which produces microwave photons. With a sufficiently low-loss cavity and high beam intensity, the emission and reabsorption of these photons produces a self-sustaining oscillation. Devices which produce this effect are known as active hydrogen masers. In order to use this effect as a clock, a quartz oscillator is phase-locked to the synthesised microwave frequency [21, 22]. Passive hydrogen masers use a lower quality factor cavity and smaller storage bulb and are thus unable to produce self-sustained oscillations, but can be produced as smaller devices [21], used, for example, in the Galileo satellite navigation [23].

Rubidium atomic clocks are available in various current designs, mainly characterised as either lamp-pumped [21] or, newer, laser pumped [24]. In the lamp-pumped design, ^{87}Rb atoms are produced in both hyperfine ground states, with the lamp providing optical pumping to deplete the population in the lower energy state and increase the population in the higher energy state. This population is simultaneously irradiated with microwaves produced by a quartz LO, which is tuned to cause a transition in the ^{87}Rb which results in greater absorption of the lamp light [21]. This combined resonance technique is known as MODR – Microwave Optical Double Resonance – and is commonly used in conjunction

with vapour cells [21]. In the laser-pumped versions, a laser diode tuned to the D_1 or D_2 optical transition of ^{87}Rb is used for the optical pumping instead of a lamp [24].

Possibly set to replace microwave frequency standard clocks in the near to mid future are optical frequency standard atomic clocks. These operate in a similar way to that indicated in fig. 1, except that a laser is used to provide the driving frequency for resonant transitions, and a frequency comb is used to down-convert the laser frequency into a useable RF output [21]. Current optical frequency standard technologies can be divided into three main types; thermal atom, optical lattice and trapped ion. Thermal atom devices are similar in concept to the CBT clocks but are based on vapour cell and atomic beam technologies and operate at much higher optical interrogation frequencies [21].

Optical lattice frequency standards use laser generated counterpropagating optical fields through a cold, neutral atomic vapour, producing dipole potential wells which trap the atoms [25]. This produces a light-atom system, which through tight confinement and the use of specific optical frequencies, Stark shifts, Doppler effects and atomic recoil can be minimised, thus providing extremely high stability across multiple timescales [25, 26].

Trapped ion optical frequency standards were surpassed in frequency stability by their optical lattice counterparts in 2014 [26], but remain effective because of their high performance and miniaturisation potential [27]. Typical devices of this type use Paul Traps to retain one or more cations by using a time-varying electric quadrupole potential to balance the ion's inertia with the coulomb force [28]. This separation of the reference atom from its environment reduces interaction with extraneous stimuli, thus increasing stability and accuracy [21].

1.2.1 Chip Scale Atomic Clocks

Current chip scale atomic clocks (CSACs) have been produced in two main design types. The least common relies on the MODR technique described above, and are essentially miniaturised versions of the laser pumped rubidium clocks, with a more advanced vertical-cavity surface-emitting laser (VCSEL) [29].

The more common approach to CSAC development is by using coherent population trapping (CPT). This development focus is due in large part to the excellent miniaturisation potential provided by the microelectromechanical system (MEMS) vapour cell and a reduced size of physics package (the detection, data processing and control circuitry) enabled by the CPT approach [30].

In CPT, two hyperfine transitions of the reference atoms are simultaneously stimulated by coherent laser radiation fields. In alkali metals, this is frequently a combination of ground state and p-state transitions, forming a so-called Λ scheme [31]. As a consequence of quantum interference, the reference medium is excited into a 'dark state', resulting in an increase of optical transmission through its containment cell, which may be detected and processed using a physics package and error correction loop [31]. As a further advantage of this system, a single modulated VCSEL can be used to produce both frequencies, resulting in direct application of microwave frequencies to the reference atoms, eliminating the requirement for a tuned resonant cavity [21]. This simplifies the build, processing and control requirements.

Whilst these devices are referred to as 'chip-scale', and whilst the cell and laser assembly fit onto a microchip sized footprint, the total size of the instrument, including the physics package, power and control equipment, is significantly larger than this.

1.2.2 Stability, Accuracy, Drift and SWaP-C

Key figures of merit for atomic clocks are those which describe the stability and accuracy of the clock, whilst figures describing its size, weight, power consumption and cost (SWaP-C) are important for application and manufacturing considerations. Stability describes how consistently a frequency standard device produces the *same* frequency over time (self-consistency), whilst accuracy is the ability of a device to produce the *correct* frequency. This latter consideration is not as simple as it might first appear: a quartz oscillator may be described as *accurate* if it faithfully produces a frequency of exactly 32768 s^{-1}, with the value of a second specified using the SI definition based on the ^{133}Cs standard. However, the optical frequency standards discussed above are proposed to have a greater accuracy than the caesium standard itself, and thus cannot be compared to it for accuracy. It is this situation that has instigated the proposal to redefine the second [17]. For the present, the systematic uncertainties of these devices are generally used for comparison and evaluation purposes.

Self-evidently, stability tends to be first and foremost in initial considerations of the effectiveness of an atomic frequency standard, and this is typically described by the Allan Deviation (ADEV):

$$\sigma_y(\tau) = \left[\frac{1}{2(M-1)} \sum_{i=1}^{M-1} (\bar{y}_{i+1} - \bar{y}_i)^2 \right]^{\frac{1}{2}}$$

(1. 1)

where

$$\bar{y}_i = \frac{x_{i+1} - x_i}{\tau}$$

(1. 2)

is the average frequency deviation over the time interval τ, and x_i are the phase differences [21, 32]. M is the number of samples taken. ADEV is the square root of the Allan Variance (AVAR), given by $\sigma_y^2(\tau)$, in a way analogous to the statistics of standard deviation and standard variance. The reason that these usual statistics cannot be used for the time domain measurements required for atomic frequency standards is that the standard deviation diverges for the flicker FM noise associated with active oscillators and their environment [33].

Typically, the ADEV for an atomic frequency standard will move through three phases with increasing time, τ [22]:

1. $\frac{1}{\alpha\tau} \leq \sigma_y(\tau) \leq \frac{1}{\tau^2}$. In the first phase, over short timescales (typically

10^4 s $< \tau < 10^5$ s) [21], $\sigma_y(\tau)$ decreases with increasing time due to the dominating influence of white (random) and flicker FM noise, and the effect of averaging, which reduces their impact.

2. $\sigma_y(\tau) \approx$ constant. This is known as the flicker floor and arises when averaging time has no further positive effect on reducing the impact of the noise.

3. $\sigma_y(\tau) = \tau^\alpha$, with $0 < \alpha \leq 1$. The ADEV begins to increase in a phenomenon known as frequency drift. The source of this can be many things but can particularly include ageing of the instrument and changes in its environment.

This typical curve is shown graphically in Figure 2 below.
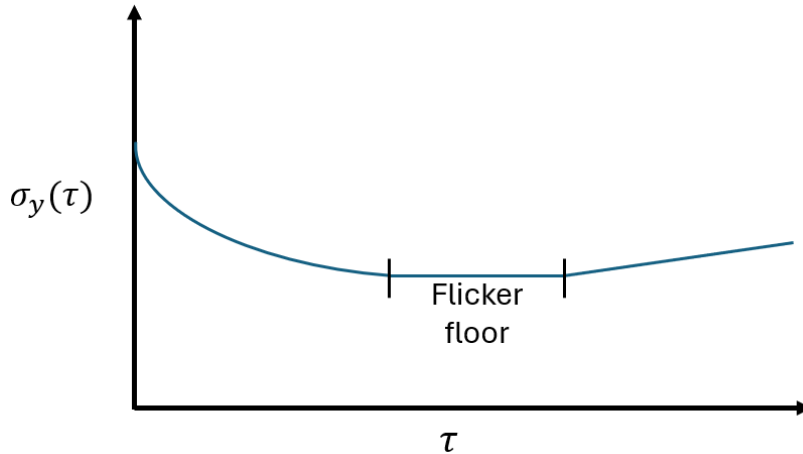
Figure 2. Typical plot of Allan Deviation against time for an atomic frequency standard.

Note that from plots of ADEV against time, it isn't possible to differentiate between contributions from white noise and flicker noise. For this reason, a modified version of the ADEV is sometimes used (MDEV), and for time error predicting purposes only, the time deviation can be used (TDEV) [21]. However, MDEV and TDEV are not frequently quoted for commercial instruments, whilst ADEV is, hence, unless noise type differentiation is critical to the matter at hand, it is simpler to use ADEV in order to make useful comparisons.

Instrument	Type	$\sigma_y(1 \text{ s})$	$\sigma_y(10^4 \text{ s})$	$\sigma_y(10^5 \text{ s})$
Microchip *SA45.s*	CSAC	3×10^{-10}	$10^{-12} < \sigma_y < 10^{-11}$	$10^{-11} < \sigma_y < 10^{-10}$
SRS *PRS10*	Rb	2×10^{-11}	$10^{-13} < \sigma_y < 10^{-12}$	$10^{-12} < \sigma_y < 10^{-11}$
Microchip *5071A*	CBT	5×10^{-12}	$\approx 10^{-13}$	$10^{-14} < \sigma_y < 10^{-13}$
Vremya *VCH-1003M*	H maser	6×10^{-14}	$\approx 10^{-15}$	$10^{-16} < \sigma_y < 10^{-15}$

Table 1. Allan Deviation of various commercially available atomic frequency standards at various averaging times. Data taken from [21].

These data clearly demonstrate the relative instability of the smaller chip scale and rubidium clocks against the larger CBT and hydrogen maser clocks: the ADEVs of the first two begin to increase by $\tau = 10^5$ s (approximately one day), whereas the CBT and hydrogen maser still have a reducing ADEV at this timescale.

Since this project aims to contribute to the production of a chip-scale atomic clock, it is instructive to consider in more detail the key metrics of existing CSAC devices, such as those in Table 2 below. Note that ageing, specified in column 3, refers to the fractional frequency change per month and differs from frequency drift inasmuch as it refers only to

internal systemic changes in the oscillator and excludes environmental and other external factors.

Instrument	$\sigma_y(1\ s)$	Ageing (month)	Size (cm³)	Weight (g)	Power (W)
Microchip *SA45.s*	3×10^{-10}	9×10^{-10}	17	35	0.12
Teledyne *TCSAC*	3×10^{-10}	3×10^{-10}	23	42	0.18
Chengdu Spaceon *CPT*	2×10^{-10}	9×10^{-10}	24	45	1.6
Accubeat *NAC*	2×10^{-10}	3×10^{-10}	32	75	1.2
Spectratime *mRO-50* (EAS)	4×10^{-11}	1.5×10^{-10}	50	75	0.36

Table 2. Comparison of key metrics of 5 commercially available chip scale atomic clocks. Reproduced from [21].

It is clear from the data that these instruments are not truly 'chip scale' in the intuitive sense, but are nevertheless highly impressive in terms of performance vs SWaP, particularly since most CBT and hydrogen maser devices range in weight from several kilograms to several tonnes. A further interesting CSAC development, not listed above due to lack of accurate performance data is the Bathys Hawaii Caesium-133 wristwatch, sold via a Kickstarter campaign in 2014 [34]. It is claimed by the manufacturer to be accurate to one second in 1000 years, although it is unclear whether this is the ADEV as shipped or an actual prediction on that timescale. At an apparent size of around 30 cm³ and with a battery requiring recharging every 30 hrs, it's more of a conversation piece that a useful watch. However, its impressive microfabrication and commercial viability indicate the growing maturity of the technology.

1.2.3 Applications and Limitations

Many applications in the modern world require extremely precise timekeeping. Global navigation satellite systems (GNSS) use triangulation of signals from or to multiple satellites in order to determine location information. The time of arrival, or difference in time of arrival, of these signals is used to calculate distance and thence location [35]. Since relativistic factors need to be taken into account, the timing underpinning these calculations must be as precise as possible to ensure useful location information. A timing error of a single microsecond can lead to a location rendering error of 300 m [36]. This requirement will continue to increase as our species becomes spacefaring, with speeds of travel and gravitational field differentials becoming more important. The White House in the USA has recently requested that NASA provide a recommendation for LTC, Lunar Coordinated Time, in order to complement UTC, since lower gravity on the moon means that clocks run ~58.7 μs/day quicker than on Earth [37].

Whilst accuracy is important, SWaP are also a significant concern. It would not be feasible, for example, to install a large caesium fountain clock or hydrogen maser, weighing >100 kg, in a satellite or spacecraft. Whilst larger clocks with greater power consumption tend to be more stable [21], compromises must be made in these, and similar circumstances. Hence, currently, for example, greater than half of all satellite-based atomic clocks in the GPS constellation are small, optically pumped rubidium standards, which are regularly calibrated for anomalies [38]. Whilst civilian ground based GNSS receivers tend to be quartz based oscillators, calibrated using a broadcast signal

(usually atomic in origin), military receivers now frequently include CSACs to ensure accurate time signal measurements [36]. This helps to mitigate the problems of signal jamming and electronic warfare [11, 36]. Such usage highlights the need for improved stability CSACs with low SWaP. Such development would also support navigation for non-military purposes, including scientific exploration and remote delivery using drones.

Similarly, geophysical sensors located underwater, underground or in other inhospitable locations with poor signal connectivity, such as those for earthquake and tsunami detection, rely on precise timing in order to synchronise data [36]. Local atomic clocks with low SWaP-C are clearly a benefit in such circumstances.

Increasingly, the internet and the rapid processing of financial transactions rely on ever more precise timekeeping in order to function with minimal error and latency [2, 39]. In the case of financial markets and trading, decisions by automated systems can occur on a microsecond timescale. It is therefore essential for equitability across all platforms, and to prevent fraud, that the timestamps associated with each transaction are maximally accurate [2]. Currently, stock exchange timing is provided by signals from the instruments contributing to TAI, but in an ever more interconnected world, where transactions can be conducted using mobile devices and satellite supported internet [40], subject to signal delays, the need for locally kept time to be as accurate and stable as possible is fast increasing.

In the light of the considerations discussed above, there is an evident need for CSACs with greater stability and lower SWaP-C. It is toward this wider purpose that the optimisations and resonance measurements detailed in this thesis are intended to contribute. An endohedral fullerene atomic clock could potentially be produced with low SWaP-C since it uses only radio frequency electronics and has *relatively* simple microfabrication requirements, without the need for vapour cells or lasers.

2. Spin Resonance

Spin resonance refers to the stimulation of the atomic energy level transitions associated with particle spin using electromagnetic illumination. Typically, microwave atomic frequency standards rely on hyperfine transitions, which involve changes in electron spin states. However, spin resonance is not limited to electrons, and other applications, such as magnetic resonance imaging (MRI), stimulate protons, whilst nuclear magnetic resonance (NMR) considers the total spin of the nucleus. Whilst this project exclusively uses EPR, many of the principles and techniques are the same or similar to those used in NMR.

Spin is considered to be intrinsic angular momentum, which in the case of protons and electrons, causes them to behave as magnetic dipoles due to the hypothetical rotational movement of their intrinsic electric charge. When they are placed in an externally applied magnetic field, a torque is experienced on the particles whose spin vectors are not aligned either parallel or antiparallel to the external field, causing them to approach alignment. In free particles unaffected by such external fields, there is no energy difference between different spin states, but in an external magnetic field, an energy gap proportional to the field strength is created between the spins, which become aligned up or down in the axis of the applied field. This is the basis of the Zeeman Effect, and can be present for unpaired electrons in the outer orbital of an atom or for protons in the nucleus. It is described by

$$\mathcal{H} = -\boldsymbol{\mu} \cdot \boldsymbol{B}$$

This is the spin Hamiltonian with which the system interacts with the magnetic field $\boldsymbol{B}$, and $\boldsymbol{\mu}$ is the spin magnetic dipole moment.

Also fundamental to the concept of spin resonance is Larmor Precession. This is analogous to the precession of the axis of rotation of a classical gyroscope in a gravitational field, and occurs because the torque, $\boldsymbol{\tau}$, exerted by the applied magnetic field, $\boldsymbol{B}$, on the magnetic dipole moment, $\boldsymbol{\mu}$, causes a change in the angular momentum vector, $\boldsymbol{J}$ as follows:

$$\boldsymbol{\tau} = \boldsymbol{\mu} \times \boldsymbol{B} = \frac{d\boldsymbol{J}}{dt}.$$

This means that the axis of $\boldsymbol{\mu}$ precesses about the field direction with a frequency called the Larmor Frequency, described by

$$\omega = \gamma B,$$

where γ is the gyromagnetic ratio of the particle or system and B is the field magnitude [42]. When a magnetic field alternating at the Larmor Frequency is applied to the particle, a resonance occurs, which can be understood in much the same way as pushing a child on a swing at exactly the right moment each time – the system is able to absorb energy at this frequency.

2.1 Electron Paramagnetic Resonance

EPR, also known as ESR (Electron Spin Resonance) is a spectroscopic technique which works through stimulation and measurement of the spin states of unpaired electrons, for example in the outer atomic orbitals of a reference medium, including free and caged radicals, and in transition metal ion complexes [11, 43]. EPR has many useful applications, the list of which is growing as the discipline evolves, and, for example, includes the investigation of the geometric and electronic structure of materials [44], electron transfer kinetics [45], manipulation of qubits [46], and of course, in the context of this thesis, potential new frequency standards.

It was first observed in 1944 by Yevgeny Zavoisky at Kazan State University [47], and at approximately the same time by Brebis Bleaney et al in Oxford, UK. EPR exploits the Zeeman effect and other forms of energy level splitting which occur as the result of interactions between electrons and the other constituent parts of the atomic or crystal structure to which they belong.

Zeeman splitting for a single electron can be described as follows.

Electrons are spin 1/2 particles with spin magnetic quantum number $m_s = +1/2$ or $m_s = -1/2$. When they are placed in a z-aligned external magnetic field, $B_0 = B_z$, spin axis alignment takes place, and hence an energy can be ascribed to each alignment state:

$$E = m_s g_e \mu_B B_0.$$

(2 4)

Here, g_e is the Landé g-factor for the electron and μ_B is the Bohr magneton, both of which are constants for a free electron. Hence, the difference in energy between the two spin states in a magnetic field can be given by

$$\Delta E = E_{m_s=+\frac{1}{2}} - E_{m_s=-\frac{1}{2}}$$

$$= g_e \mu_B B_0.$$

(2 5)
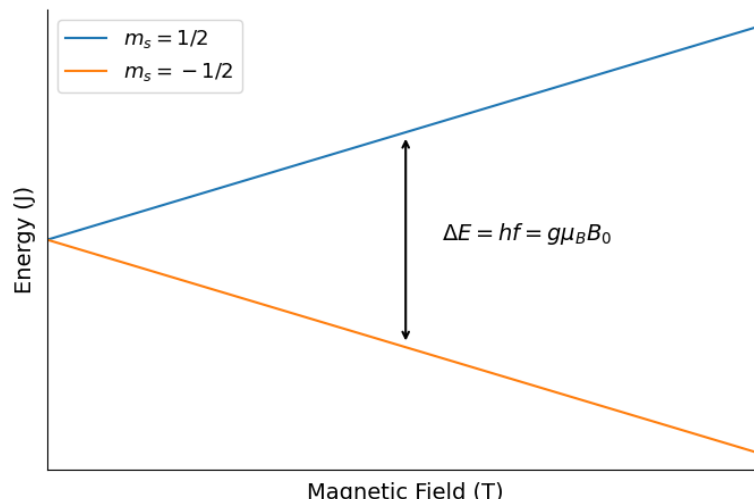
Figure 3. Zeeman splitting for a single electron in a magnetic field. The energy gap is shown to increase with increasing field strength.

The extra term, $\Delta E = hf$, indicates the basic principle of EPR, in which electromagnetic radiation may be applied with frequency

$$f = \frac{g_e \mu_B B_0}{h}$$

in order to provide the correct amount of energy to the electron in the lower energy state to transition to the higher energy state. Alternatively, this may be expressed as

$$f = \frac{\gamma_e}{2\pi} B_0$$

where γ_e is the electron gyromagnetic ratio. This is the Larmor precession frequency described above [42].

It is important to note that due to the quantized nature of the states, only a frequency of precisely this value will cause the resonant transition. Typically, in EPR spectroscopy, this energy is provided by an oscillating magnetic field, B_1, usually produced using a resonant microwave cavity (as in the examples of atomic frequency standards above) or a loop gap resonator [48], which will be discussed in greater detail below.

Whilst the above is instructive as to the underlying principle, in real atoms and molecules, the electrons are not free. The reason that EPR is only applicable to atomic structures with unpaired electrons is that the spins of paired electrons in 'full' orbitals are not free to change. Electrons occupy orbitals in an atomic structure following the Aufbau principle and Hund's Rules. Hence, inner orbitals are always occupied first, and the outer orbitals are initially singly occupied prior to hosting pairs of spin-opposite electrons. The Pauli exclusion principle means that no two electrons can occupy the same quantum state in any atom. Atoms 'want' to be electrically neutral, and so balance the number of electrons with the number of protons in the nucleus. This means that some atoms, such as the Nitrogen-15 studied in this thesis, remain in a state with unpaired electrons in the outermost orbital.

However, these electrons do not behave in the same way as free electrons outside an atomic structure. They are subject to various interactions involving angular momentum and charge which must be taken into account when considering what the resonant frequencies of a reference medium will be. These can be described as follows.

Spin orbit coupling describes the interaction of the spin and orbital angular momenta of the electron, and leads to the fine structure in the energy levels of an atom. The component of the relevant spin Hamiltonian will have a term, $\mathcal{H} \propto \boldsymbol{L} \cdot \boldsymbol{S}$, where $\boldsymbol{L}$ and $\boldsymbol{S}$ are the orbital and spin angular momentum vectors respectively.

Hyperfine coupling describes the interaction of the electron with the nucleus, both in terms of the Fermi contact interaction (FCI) and magnetic dipole coupling (MDC). The FCI concerns the overlap of the electron and nuclear wavefunctions, whilst MDC concerns the interaction between the magnetic dipoles of the electrons and nucleons. This creates the hyperfine structure of energy levels in an atom. It is described by spin Hamiltonian,

$$\mathcal{H} = \boldsymbol{S} \cdot \widehat{\boldsymbol{A}} \cdot \boldsymbol{I}$$

where $\boldsymbol{S}$ and $\boldsymbol{I}$ are the electron and nuclear total spins, and $\widehat{\boldsymbol{A}} = \widehat{\boldsymbol{A}}_{FCI} + \widehat{\boldsymbol{A}}_{MDC}$ is the hyperfine coupling tensor [49].

Zero field splitting refers to the coupling of electron spins to each other and can occur in atoms with more than one unpaired electron. It is also called dipolar coupling, hence its representation by the spin Hamiltonian, $\mathcal{H} = \boldsymbol{S} \cdot \widehat{\boldsymbol{D}} \cdot \boldsymbol{S}$, where $\widehat{\boldsymbol{D}}$ is a matrix describing the interactions.

Quadrupolar coupling similarly describes the self-coupling of the nucleon magnetic fields and can only occur where the total nuclear spin magnitude $I > 1/2$. This is true only for nuclei with non-spherical charge distribution [49]. It is for this reason that nitrogen-15 is used in the reference medium for the experiments in this thesis rather than the more common nitrogen-14. The extra neutron in ^{15}N means that $I = 1/2$ and thus removes the complication of further splitting due to a quadrupolar coupling. Quadrupolar coupling can be described by a spin Hamiltonian, $\mathcal{H} = \boldsymbol{I} \cdot \widehat{\boldsymbol{Q}} \cdot \boldsymbol{I}$.

Zero field splitting and splitting due to quadrupolar coupling are also frequently referred to as forms of hyperfine splitting.
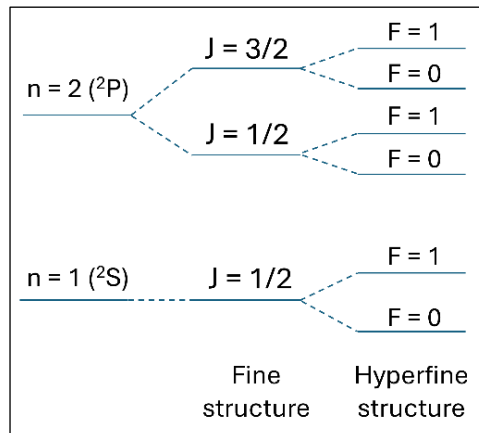
Figure 4. Schematic diagram of the hyperfine splitting in the hydrogen atom. Recreated from [50].

The hyperfine energy level manifold of ^{15}N@C$_{60}$ will be discussed later in this document, but the schematic in Figure 4 shows a simple example of hyperfine structure in the hydrogen atom. Here, n is the principal quantum number, referring to the energy levels of an electron in the atom, $J = |\boldsymbol{J}| = |\boldsymbol{L} + \boldsymbol{S}|$, is the total electron angular momentum, and $F = |\boldsymbol{F}| = |\boldsymbol{I} + \boldsymbol{J}|$ is the total angular momentum of the atom. The levels arise since hydrogen has a single proton as a nucleus and a single electron, both of which are spin $\frac{1}{2}$ particles.

2.2 EPR Methods

EPR spectroscopy is split into two main methodologies – continuous wave EPR (CW EPR) and pulsed EPR. More complex methodologies also exist which combine techniques with other disciplines, such as ENDOR – electron nuclear double resonance [51], and LITTER -

light-induced triplet–triplet electron resonance spectroscopy [52]. The experiments detailed in this thesis use CW EPR exclusively, hence that will be the focus of this document.

As the name suggests, CW EPR involves applying continuous electromagnetic illumination to the reference medium. Typically, the reference medium is located within a resonator device, which is then contained within an apparatus designed to produce a homogeneous magnetic field, B_0. The resonator is connected to control apparatus which electrically stimulates the device to produce an oscillating magnetic field, B_1, at the desired frequency to drive the transitions. B_1 is applied continuously to the sample, whilst B_0 is swept over a range which includes the expected resonances, that is, the combination of B_1 and B_0 which will allow absorption of the energy provided by B_1.

The resonator control apparatus will include detection circuitry which involves measuring changes in the resonator's electrical coupling characteristics due to the absorption and will return a spectrum similar to the example in Figure 5 below.
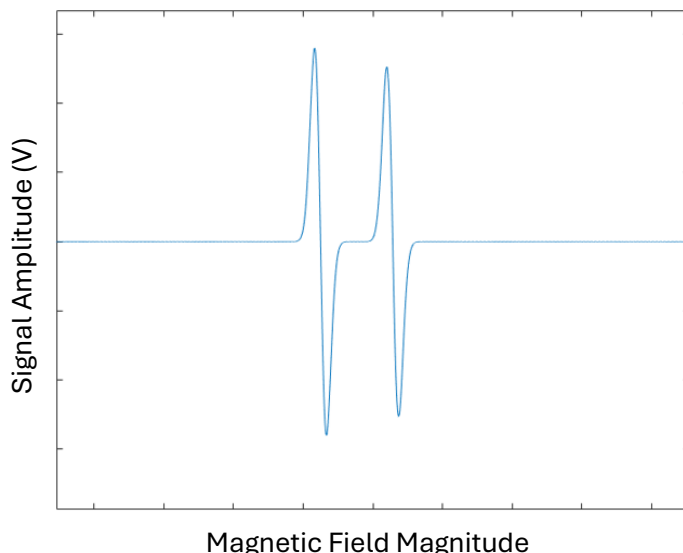
Figure 5. Example field domain EPR spectrum produced using EasySpin in MATLAB.

In practice, the signal amplitude is often low in comparison to the noise in the system, and so a further oscillating magnetic field, B_{mod}, is used to modulate B_0 so that a method of phase sensitive detection, such as a lock-in amplifier, can be used to extract the resonance signal by amplifying only those components of the total signal which oscillate at the modulation frequency. This works because the spins in the reference medium respond to the field modulation, whilst the rest of the electronics do not, or at least do so only minimally.

In pulsed EPR, it is easier to consider the net magnetisation vector (M_0) of the reference medium sample than individual spins. At room temperature, the Boltzmann Distribution indicates that a majority of the electron spins in the sample will be in the parallel spin state with respect to B_0 (precessing at the Larmor frequency), since this is the lower energy state. One can therefore describe M_0, which is the vector sum of all the individual spins in the sample, and will thus be aligned with the B_0 axis. M_0 can then be manipulated using pulses of electromagnetic radiation, provided by B_1, using apparatus similar to that used for CW EPR.

If one considers a rotating reference frame synchronous with the Larmor precession of the electron spins as a result of $\boldsymbol{B}_0$, then, $\boldsymbol{B}_1$, in the resonance condition, will cause a precession of $\boldsymbol{M}_0$. This is called the Rabi frequency and is given by

$$\omega_r = -\gamma B_1,$$

where $B_1 = |\boldsymbol{B}_1|$. During pulses of $\boldsymbol{B}_1$, $\boldsymbol{M}_0$ will rotate around the $\boldsymbol{B}_1$ axis, at an angle given by

$$\theta = -\gamma B_1 t_p,$$

where t_p is the pulse duration. The pulses used in this methodology are frequently described by this angle, for example, a $\frac{\pi}{2}$ pulse is when $\theta = \frac{\pi}{2}$. Off resonance, the calculations are slightly more complex but follow similar reasoning.

The precession described above can be measured in the apparatus in the stationary laboratory reference frame by using a wire coil, oriented appropriately with reference to θ, so that the changing magnetic field induces an electrical current. The precession, ω_r, and tip angle, θ, will decay in the absence of $\boldsymbol{B}_1$, in a phenomenon known as free induction decay (FID), shown in Figure 6 below.
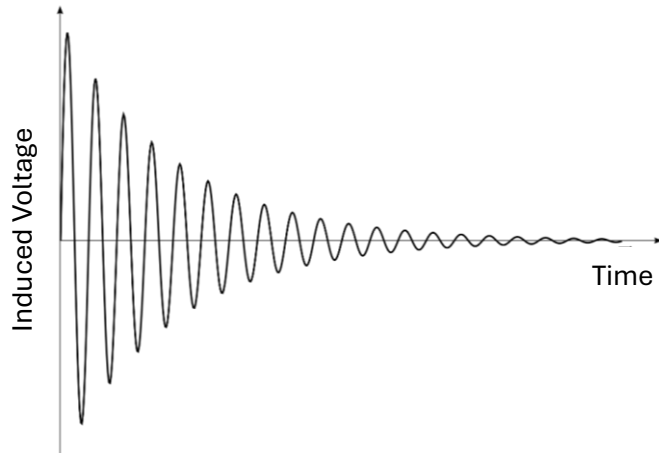
Figure 6. Voltage produced in a solenoid over time by free induction decay. Reproduced from [53].

FID is characterised by the spin-lattice relaxation time, T_1, and the spin-spin relaxation time, T_2, and hence can be used, along with more advanced techniques, such as spin echo, to accurately determine these times for the sample at hand. T_1 is the time taken for $\boldsymbol{M}_0$ to return to the $\boldsymbol{B}_0$ axis, and T_2 is the time taken for the net magnetisation in the plane perpendicular to the $\boldsymbol{B}_1$ axis to disappear. These relaxations occur due to the electrons interacting with each other and their environment. Understanding them can give insights into the structure and dynamics of atomic and molecular systems.

The further techniques of pulsed EPR and related disciplines are beyond the scope of this thesis.

3. Experimental CW EPR for this Project

The technique and methodology for using EPR with endohedral fullerenes as the basis for an atomic frequency standard CSAC was proposed by Andrew Briggs and Arzhang Ardavan at the University of Oxford, in 2008 [11]. It has since been pursued and developed by Edward Laird and Kyriakos Porfyrakis [11], Reuben Harding et al [49, 54], Matthew Green [55], and Scott Henderson [56]. This thesis seeks to both build upon and contribute to their work by demonstrating instrumental improvements, refining existing data and offering new data to support the concept of using ^{15}N@C$_{60}$ in this way.

3.1 The Endohedral Fullerene ^{15}N@C$_{60}$

Endohedral fullerenes are molecules consisting of a cage of carbon atoms, bonded to each other, with an atom of a different element contained inside. ^{15}N@C$_{60}$ contains a ^{15}N atom inside a C$_{60}$, or Buckminster Fullerene, outer cage. Its synthesis was first reported by Murphy et al in 1996 [57], who deduced that EPR measurements of the molecule would correspond almost exclusively to the paramagnetic ^{15}N, since the C$_{60}$ cage is diamagnetic. This was the first time that atomic nitrogen could be studied alone, since its 3 unpaired p-orbital electrons, which make it suitable for EPR, ensure that it is highly reactive under normal conditions. The neutral C$_{60}$ cage effectively isolates the nitrogen atom, preventing reactions and interactions, meaning that the molecule retains the expected ^{15}N total electron spin $S = 3/2$.

Murphy et al were able to confirm the expectation that ^{15}N has an isotropic hyperfine constant, and measured the value to be $|A|/h = 22.021$ MHz [57]. This is approximately 50% larger than the measured value of individual atomic nitrogen, an effect thought to be caused by the restriction of the trapped nitrogen's electron cloud within the cage [57]. This was confirmed by Pietzak et al [58], who measured the hyperfine constant to be $|A|/h = 22.35(3)$ MHz. More recent measurements of $|A|/h$ have yielded results within this range: 22.26 MHz [59], and 22.277 ± 0.001 MHz [54]. Part of the work detailed in this thesis has been to confirm these data and provide further constraint on this constant.
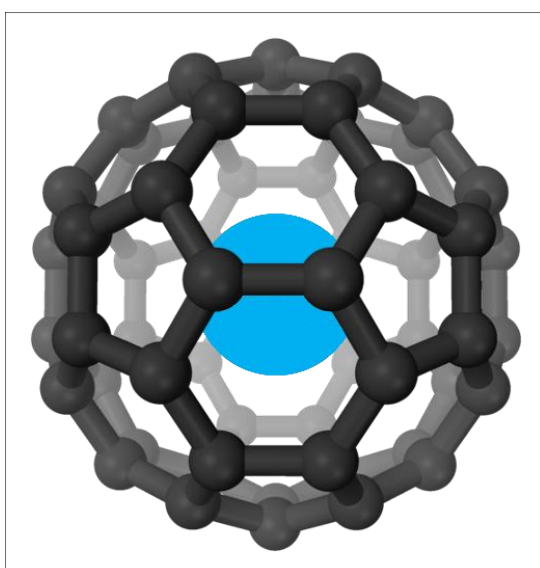

Figure 7. Illustration of ^{15}N@C$_{60}$, created using [60]. This shows the Nitrogen-15 atom (blue) encapsulated in the Carbon-60 cage. (Not to scale).

As mentioned above, ^{15}N@C$_{60}$ has no quadrupolar coupling. Furthermore, zero field splitting can be neglected due to the approximately spherically symmetric nature of the atom [54, 61]. There is no spin-orbit coupling since this is proportional to $\boldsymbol{L} \cdot \boldsymbol{S}$, with the total angular momentum, $L = 0$ for the p-orbital electrons in this molecule.

This gives a Hamiltonian for the molecule containing only Zeeman splitting terms and a Hyperfine splitting term, as below, given for the case of a z-facing applied magnetic field, $\boldsymbol{B}_0 = B_0 \hat{z}$:

$$\mathcal{H} = g_e \mu_B S_z B_0 - g_N \mu_N I_z B_0 + A \widehat{\boldsymbol{S}} \cdot \widehat{\boldsymbol{I}}$$

<div align="right">(3. 1)</div>

Here, g_e and g_N are the electron and nuclear g-factors; μ_B and μ_N are the Bohr and nuclear magnetons; S_z and I_z are the electron and nuclear spin components in the z-direction; A is the isotropic hyperfine constant; $\widehat{\boldsymbol{S}}$ and $\widehat{\boldsymbol{I}}$ are the electron and nuclear spin operators [54]. By expressing the nuclear magnetic moment using the Bohr magneton as $g_I \mu_B = g_N \mu_N$, the Hamiltonian can be alternatively written as

$$\mathcal{H} = g_e \mu_B S_z B_0 - g_I \mu_B I_z B_0 + A \widehat{\boldsymbol{S}} \cdot \widehat{\boldsymbol{I}}$$

<div align="right">(3. 2)</div>

From this Hamiltonian, the energy eigenvalues can be extracted with the following forms, where $g_{tot} = g_e + g_I$, (from [61]):

$$E_1 = \left(\frac{3}{2} g_e - \frac{1}{2} g_I \right) \mu_B B_0 + \frac{3}{4} A,$$

<div align="right">(3. 3)</div>

$$E_{2,3} = g_e \mu_B B_0 - \frac{A}{4} \pm \frac{1}{2} [(g_{tot} \mu_B B_0)^2 - 2 g_{tot} \mu_B B_0 A + 4A^2]^{\frac{1}{2}},$$

<div align="right">(3. 4)</div>

$$E_{4,5} = -\frac{A}{4} \pm \frac{1}{2} [(g_{tot} \mu_B B_0)^2 + 4A^2]^{\frac{1}{2}},$$

<div align="right">(3. 5)</div>

$$E_{6,7} = -g_e \mu_B B_0 - \frac{A}{4} \pm \frac{1}{2} [(g_{tot} \mu_B B_0)^2 + 2 g_{tot} \mu_B B_0 A + 4A^2]^{\frac{1}{2}},$$

<div align="right">(3. 6)</div>

$$E_8 = \left(-\frac{3}{2} g_e + \frac{1}{2} g_I \right) \mu_B B_0 + \frac{3}{4} A.$$

<div align="right">(3. 7)</div>

A plot of the energy eigenvalues with applied magnetic field strength is displayed in Figure 8 below, where it should be noted that the negative value of the nuclear g-factor leads to a negative value of A and an inverted energy manifold [54, 61].

When $\boldsymbol{B}_1$ is parallel to $\boldsymbol{B}_0$, ^{15}N@C$_{60}$ has a clock transition at an anticrossing between energy levels 6 and 7 (given by equations 3.6 above) [54, 61]. Such transitions are so called because they provide the greatest suitability for use in an atomic clock. The reason for this can be seen clearly in Figure 9 below; when the resonant frequencies are plotted with respect to applied magnetic field ($\boldsymbol{B}_0$), strength, it can be seen that at the bottom of the parabola describing E_{67}, $df/(dB_0) = 0$. This gives the benefit that a clock utilising this frequency as its reference will be less sensitive to small extraneous disturbances in magnetic field, leading to greater frequency stability.
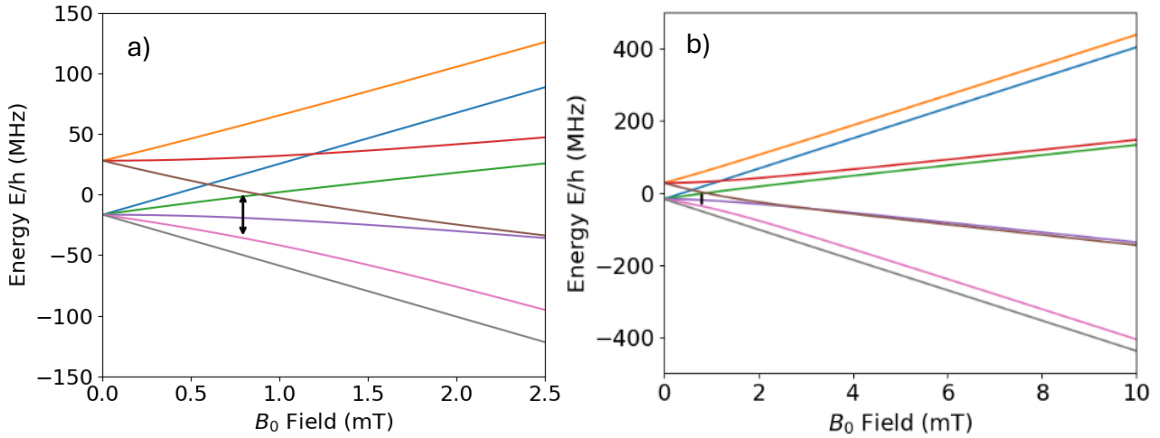
Figure 8. The Hyperfine energy level splitting of ^{15}N@C$_{60}$ at low (a) and high (b) field strength. The clock transition is shown by the black arrow (a) and line (b). At higher fields the Zeeman splitting dominates and the levels become 4 sets of hyperfine split doublets.
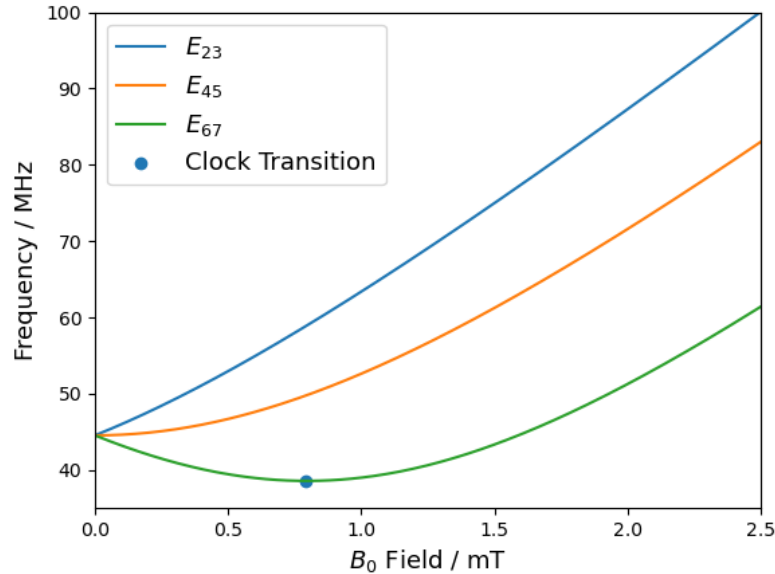
Figure 9. Resonance frequencies of ^{15}N@C$_{60}$ with $\boldsymbol{B}_1 \parallel \boldsymbol{B}_0$, showing the clock transition.

The following values were used to create the plots in Figures 8 and 9:

$$\frac{A}{h} = -22.2695 \; MHz$$

$$g_e = 2.00232$$

$$g_I = -0.00031$$

This value for the hyperfine constant is used here because it is the most accurate value obtained to date in the experiments detailed below. A different set of resonant frequencies occur when $B_1 \perp B_0$, due to the fact that different transitions between energy levels are allowed/disallowed in this perpendicular mode. The experiments detailed in this thesis use only the parallel mode plotted here, $B_1 \parallel B_0$, primarily because the clock transition is only allowable in this arrangement.

Using the above parameters, the clock frequency (the resonant frequency pertaining to the clock transition) is ~38.57 MHz, and occurs at low field (<1 mT). This simplifies the use of the molecule in a CSAC environment because the interrogation equipment can be limited to relatively simple radio frequency electronics and a low power electromagnet, avoiding the need for lasers and vapour cells, which use a significant amount of power in operation, are difficult to manufacture, and can be fragile in use and prone to age-related degeneracy of the micro-manufactured components [62].

The EPR spectrum of $^{15}N@C_{60}$ has been shown to have a narrow frequency domain linewidth, which sharpens in particular toward the clock transition [54] when considered in the field range plotted in Figure 9. This will be explored further in the experimental data below, but important for consideration here is the effect on the suitability of the molecule as an atomic frequency reference. The frequency domain linewidth refers to the absorption magnitude curve plotted across a range of frequencies. A narrower width means that the gradient of the curve is steeper, in turn meaning that in a CSAC application, if the driving frequency from the LO drifts, there will be a greater change in absorption magnitude and a fast error correction response.

The endohedral fullerenes used in this experiment were made in Oxford by Designer Carbon Materials using ion implantation and high pressure liquid chromatography (HPLC) [11]. The fullerenes are vapourised and deposited onto a copper sheet prior to being bombarded with ^{15}N. The penetration rate of the nitrogen into the C_{60} is approximately 0.01%, and so the bombarded fullerenes are passed through the HPLC process, where the carbon cages containing ^{15}N are separated from the empty ones via tiny differences in polarizability and molecular weight. This is a long and intensive process which makes $^{15}N@C_{60}$ very expensive to produce – a limitation which must be overcome in order to create a commercially viable CSAC.

To enable the use of $^{15}N@C_{60}$ in our spectrometer, it is dissolved in deoxygenated carbon disulfide and placed into a vacuum tube. Excess CS_2 is boiled off using a vacuum pump until the solution reaches approximate saturation, occupying around $1cm^3$, which ensures the correct filling factor for the resonator (see 3.2 below). The tube is then flushed with argon and sealed, ensuring no oxygen is present inside and the spin signal is restricted to the paramagnetic centres of the $^{15}N@C_{60}$. CS_2 is used because it does not react with the C_{60} cages and does not interfere with the EPR signal.

Approximately 1.5 mg of a $^{15}N@C_{60}$ sample of purity 22,000 ppm (referring to the number of endohedral fullerenes out of the total number of fullerene cages) dissolved in 1 cm^3 of CS_2 was used in the experiments detailed in section 4. The exact quantity of fullerenes is not known due to a problem which occurred in preparation. However, measurements with the spectrometer indicated that the spin density was approximately equal to a known 5 mg sample of 6,500 ppm purity in 1 cm^3 of CS_2.

In summary, the above facts demonstrate that $^{15}N@C_{60}$ is suitable for use as an atomic frequency standard for a CSAC application:

- Available in a simple liquid solution,
- Stable at room temperature,
- Radio frequency clock transition at low magnetic field,
- Narrow linewidth,
- Easily miniaturisable.

The main contra-indication for CSAC usage is the high cost of manufacture, however, it is envisaged that this could be reduced by economies of scale and investment in industrialisation of the process. There are also temperature [63] and pressure [49] sensitivities associated with the molecule which could potentially cause problems in some applications, e.g. spacecraft and military applications. These factors are yet to be fully explored in their relevance to CSAC operation and lie outside the scope of this thesis.

3.2 Instrumentation and Methods

All experiments in this thesis were conducted using a benchtop CW EPR spectrometer constructed from components, instruments and individually designed, 3D printed and machined parts. The latter were designed and manufactured by the project team and technicians within the university. A circuit diagram of the base spectrometer setup is given in Figure 10.
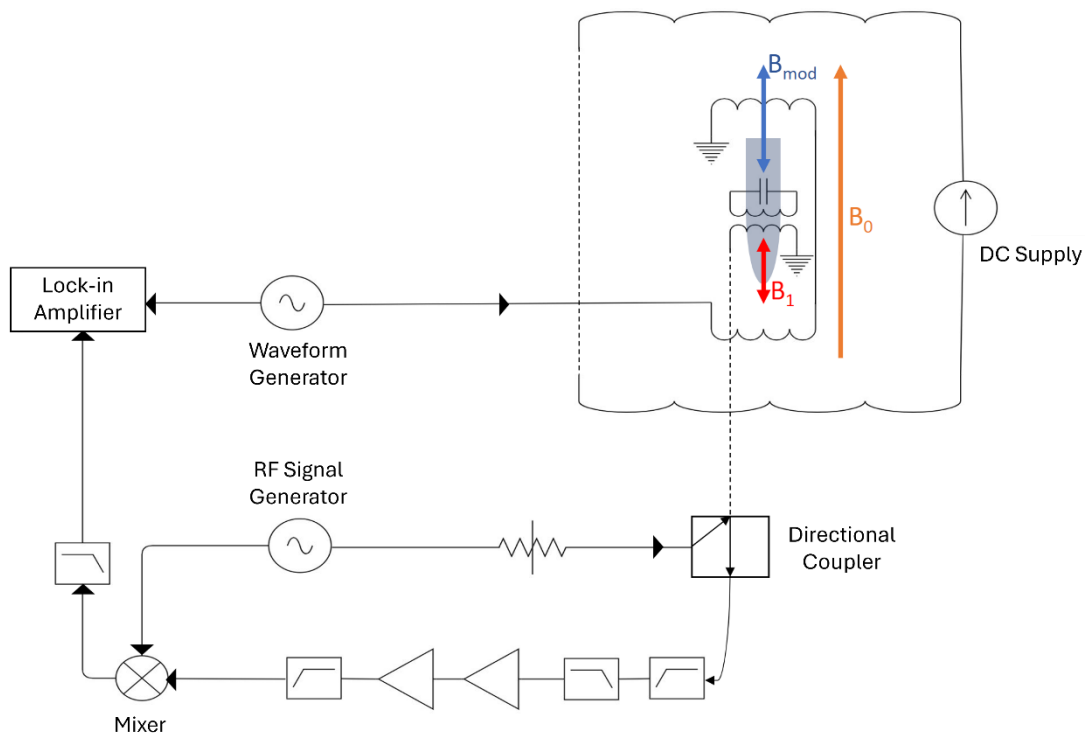

Figure 10. EPR Spectrometer circuit diagram. Note that coils are shown as inductors at 90° to convention to best emulate the physical setup.

The reason for building a bespoke spectrometer is that no commercial unit was available for performing experiments in the frequency range required. Most commercial spectrometers use microwave cavities as resonators, however the wavelength of our clock

transition frequency is ~7.8 m, which would require an enormous cavity to facilitate the electromagnetic resonance.

The spectrometer works using the principles of radio frequency reflectometry [64], acquiring the first derivate of the absorption signal from a field-swept measurement. The swept field, $\boldsymbol{B}_0 = B_0\hat{z}$, is generated using a variable DC supply connected to a Helmholtz coil set. This ensures maximal field homogeneity for the sample, which is placed at the central point on the Helmholtz pair axis, inside a machined aluminium cavity for shielding. To the inner cavity walls are fixed smaller modulation coils, two for parallel mode and two for perpendicular mode operation. These are in pairs which can be approximated using the Helmholtz equations, although their separation is in fact slightly larger than such a configuration. These coils provide the modulation field; $\boldsymbol{B}_{mod} = B_{mod}\hat{z}$ for parallel mode, and are driven by a waveform generator producing a sine wave of ~6 kHz.

The transitions are driven using an RF signal generator. This outputs into a splitter, one output from which passes through a variable attenuator and directional coupler to a coupling loop attached to a platform inside the sample cavity (see below). This is a single loop of wire, shorted so that the centre of the coaxial transmission line is connected directly to the outer. The coupling loop is inductively coupled to the resonator, which generates the oscillating drive field, $\boldsymbol{B}_1 = B_1\hat{z}$. Typically, the coupling loop and resonator are critically coupled (as closely as possible) by moving the loop up and down the z-axis (using a differential screw attached to the loop platform) until the resonator is impedance matched to the rest of the circuit. The coupling process is undertaken with a vector network analyser (VNA) connected to the coupling loop via the coaxial input cable, whilst sweeping frequency across the resonator's electrical resonance. A power loss from the loop of $> |-70 \text{ dB}|$ is taken to be the closest to critical coupling achievable. The resonator is an RLC circuit, with resonant angular frequency $\omega = \frac{1}{\sqrt{LC}}$.

On resonance, the magnetic susceptibility of the sample modifies the impedance of the resonator such that it is no longer impedance matched to the transmission line, and a portion of the signal input power is reflected at the coupling loop. This reflected signal travels back down the coaxial cable, through the directional coupler and the filter and amplifier chain, configured with a band pass of 27.5 – 48 MHz and 46 dB gain.

The mixer is in a homodyne arrangement in that it receives a signal from the RF generator and mixes this with the spin-modulated signal. The resulting output is a signal oscillating at the modulation frequency (6029 Hz), which is then passed via a 10 kHz LPF into a lock-in amplifier. The lock-in uses a signal from the waveform generator in order to demodulate the signal down to DC, which is the signal we report via the lock-in's data acquisition function. A lock-in amplifier is used because the spin absorption signal is in fact much smaller than the noise in the circuit. Only the spins respond to the modulation frequency, since it varies the value of $\boldsymbol{B}_0$ which they experience, and so extracting signal components at this frequency allows noise to be rejected.

The instrument control, data acquisition and plotting is undertaken using Python code and APIs, which are either drivers written in the QCodes module format, or in the case of the lock-in, using Zurich Instruments' proprietary API. Full instrument and component specification is given in appendix 1, and the mathematical derivation of the signal acquisition is given below.
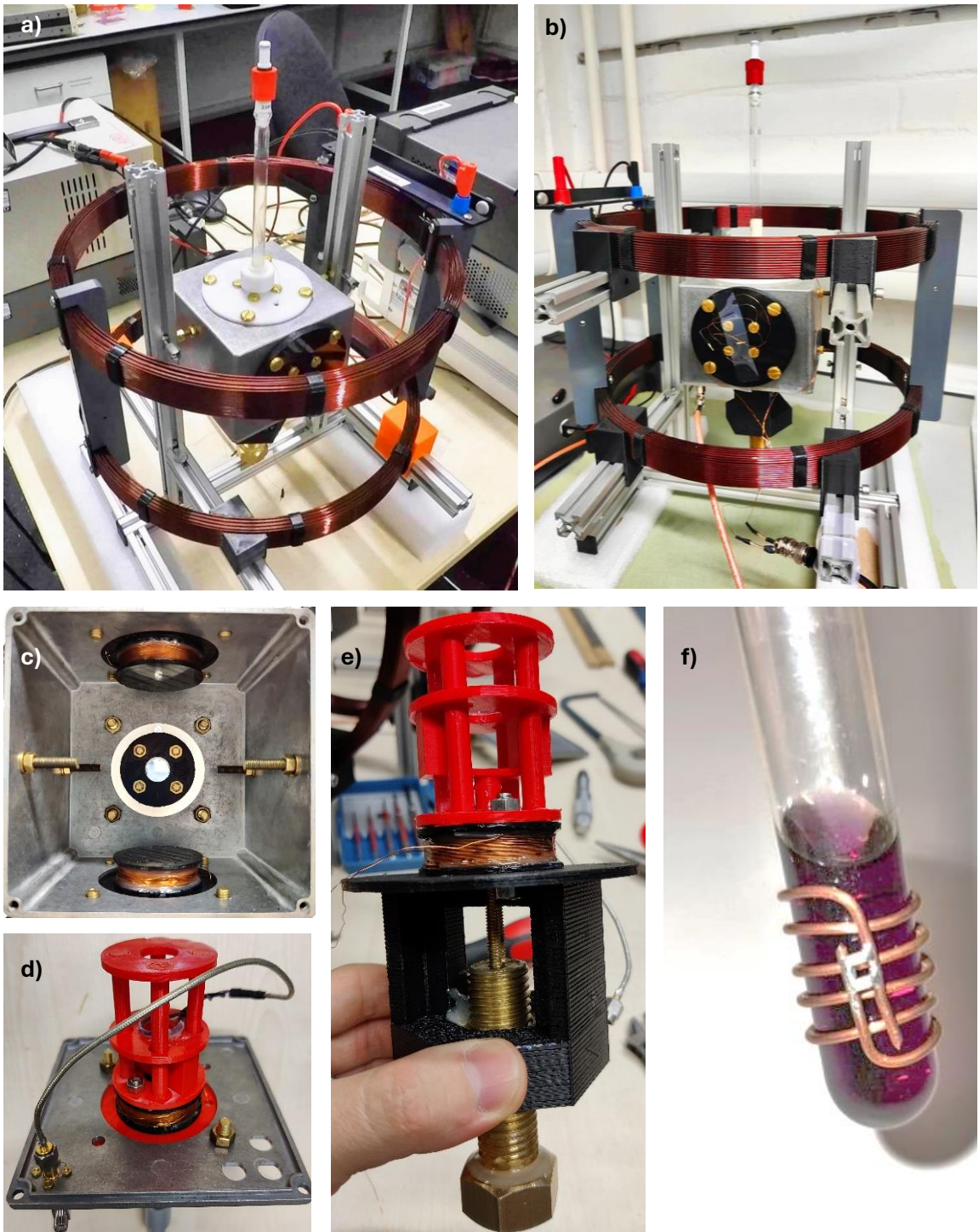
Figures 11. a) & b) Two views of the spectrometer showing the Helmholtz coils and inner cavity with the sample vacuum tube inserted. The tube is fixed in place using the threaded white piece in the photo which compresses a plastic clamp onto the tube surface. c) The inner cavity, showing perpendicular modulation coils. d) The coupling loop on its moveable platform, attached to the removed bottom plate of the inner cavity. e) The differential screw assembly connected to the coupling loop platform, showing one of the parallel mode modulation coils. f) A resonator fitted to the sample tube. Note that in this photograph, the resonator and sample volume in the tube had not been optimised.

The photographs in Figure 11 above show the spectrometer and instrumentation. More detail on the resonators and differential screw are given in section 4. The Helmholtz coils and inner cavity are suspended on an aluminium sectional framework. Non-magnetic screws and fastenings are used throughout, and the frame, cavity walls and ground terminal of the coupling loop are connected to ground via the coaxial sheath connected to the coupling loop. This is separate from the grounding of the modulation coils, as I found that this configuration reduced overall noise in the signal. Autodesk Inventor Pro CAD package was used to design the plastic parts, which were 3D printed using PLA or ABS in the university mechanical workshop. Where any deviation from this base setup was required, the changes are detailed in the relevant part of section 4.

3.3 Homodyne Mixing and Demodulation

The mixer, and the first phase of processing by the lock-in amplifier, are homodyne mixing arrangements, whereby a reference signal is used which has the same frequency as the signal of interest. Effectively, the mixer multiplies the signal and reference together to obtain a DC output whose amplitude is proportional to that of the signal.

This can be understood mathematically in the following way [55]. We begin with the two inputs to the mixer: the signal input, V_s, and the reference, V_r, given by

$$V_s(t) = V_s \cos(\omega_s t) + \sum_{n=1} V_n \cos(\omega_n t)$$

(3. 8)

$$V_r(t) = V_r \cos(\omega_r t + \phi),$$

(3. 9)

where all phase components are collected in ϕ. V_s contains noise acquired from the various steps in the circuit of various frequencies and amplitudes, represented by the summation on the RHS. Multiplying these signals gives the output of the mixer as follows:

$$
\begin{aligned}
V_{out} &= V_s(t) \times V_r(t) \\
&= V_s \cos(\omega_s t) \cos(\omega_r t + \phi) + \sum_{n=1} V_n \cos(\omega_n t) \cos(\omega_r t + \phi) \\
&= \frac{V_s}{2} \big[\cos((\omega_s + \omega_r)t + \phi) + \cos((\omega_s - \omega_r)t - \phi)\big] \\
&\quad + \sum_{n=1} \frac{V_n}{2} [\cos((\omega_n + \omega_r)t + \phi) + \cos((\omega_n - \omega_r)t - \phi)].
\end{aligned}
$$

(3. 10)

Using a low pass filter with a judiciously selected frequency will remove almost all components with additions in frequency and higher harmonics. This will also remove many noise components where $\omega_n \gg \omega_r$. Further, in a homodyne setup, $\omega_s = \omega_r$. This results in a DC component of the output proportional to phase as follows:

$$V_{out} = \frac{V_s}{2}\cos((0)t - \phi) + \sum_{n=1} \frac{V_n}{2}\cos((\omega_n - \omega_r)t - \phi)$$

$$= \frac{V_s}{2}\cos(\phi) + \sum_{n=1} \frac{V_n}{2}\cos((\omega_n - \omega_r)t - \phi)$$

(3. 11)

where the identity $\cos(-\phi) \equiv \cos(\phi)$ has been used. A high pass filter used prior to the mixer will remove many noise components where $\omega_n < \omega_s$, leaving the ratio of amplitudes V_s/V_n as high as possible. The DC component can then be selectively amplified and measured, giving the measurement signal, V_{meas}, as

$$V_{meas} = D\frac{V_s}{2}\cos(\phi),$$

(3. 12)

where D is the amplification factor.

The problem here is that the amplitude of the signal is proportional to ϕ. Hence, in a lock-in amplifier, there is an additional step. The reference signal is split in two, with one branch phase shifted by $\pi/2$, giving two references:

$$V_X(t) = V_r \cos(\omega_r t + \phi);$$
$$V_Y(t) = V_r \sin(\omega_r t + \phi).$$

(3. 13)

After mixing, this results in two output quadratures,

$$X = DV_s V_r \cos(\phi);$$
$$Y = DV_s V_r \sin(\phi).$$

(3. 14)

The phase can be removed and a magnitude obtained using $R = DV_s V_r = \sqrt{X^2 + Y^2}$, and the phase can be examined using $\phi = \tan^{-1}(Y/X)$. This is used in the spectrometer to demodulate the signal at the modulation frequency produced by the waveform generator. In practice, the phase is adjusted so that all of the signal is the X quadrature.

3.4 Signal Derivation

To describe the signal acquired and plotted in the experiments in this thesis, it is best to consider the interaction between the sample and the applied magnetic fields from the semi-classical rather than the quantum viewpoint. In doing so, we consider the magnetic susceptibility of the sample, which is a measure of the degree to which it becomes magnetised in an external magnetic field. This can be thought of as the totality of the spin responses. The magnetic susceptibility, χ, can be described as a combination of its dispersion, χ', and absorption, χ'', components, $\chi = \chi' + \chi''$. The derivation of the measured signal from the spectrometer can then be described as follows (reproduced and adapted from [55]).

On resonance, the magnetic susceptibility alters the impedance of the bare resonator, L_0, such that its inductance can be given as

$$L = L_0(1 + \eta\chi' + i\eta\chi''),$$

where η is the filling factor of the resonator, parametrising the degree to which the sample fills the resonator volume [49]. The reflected portion of the signal received at the mixer (neglecting the noise components for simplicity) can then be given as

$$V_s = \mathcal{Re}\big(\chi e^{i\omega t}\big) = \mathcal{Re}\left((\chi' + i\chi'')e^{i\omega t}\right).$$

Noting the above process for homodyne mixing, temporarily neglecting the field modulation, and expanding V_s into trigonometric form using Euler's formula, the output from the mixer can be given as:

$$
\begin{aligned}
V_{mix} &= D\cos(\omega t + \phi) \times V_s \\
&= D\cos(\omega t + \phi) \times \mathcal{Re}[\chi'\cos(\omega t) - \chi''\sin(\omega t) + i(\chi'\sin(\omega t) + \chi''\cos(\omega t))] \\
&= D\cos(\omega t + \phi) \times [\chi'\cos(\omega t) - \chi''\sin(\omega t)] \\
&= \frac{D}{2}[\chi'\cos(\phi) + \chi'\cos(2\omega t) - \chi''\sin(\phi) - \chi''\sin(2\omega t + \phi)].
\end{aligned}
$$

This passes through a low pass filter, leaving

$$V_{mix,LPF} = \frac{D}{2}(\chi'\cos(\phi) - \chi''\sin(\phi)).$$

The magnetic susceptibility terms can be written as modifiers of a Lorentzian distribution, $f(\omega)$, with respect to frequency, where

$$f(\omega) = \frac{1}{\pi}\frac{\frac{1}{2}\delta\omega}{(\omega - \omega_0)^2 + \left(\frac{1}{2}\delta\omega\right)^2}.$$

Here, ω_0 is the resonant frequency and mean frequency of the distribution, and the full width at half maximum (FWHM) is given by $\delta\omega$. We can then express χ' and χ'' as follows:

$$
\begin{aligned}
\chi' &= -\frac{\pi}{2}\chi_0\omega_0(\omega - \omega_0)\frac{1}{\frac{1}{2}\delta\omega}f(\omega) \\
\chi'' &= \frac{\pi}{2}\chi_0\omega_0 f(\omega),
\end{aligned}
$$

where χ_0 is the susceptibility constant. Substituting these values into equation (3.17) leads to an equation for the signal, which is a Lorentzian distribution modified by a phase:

$$V_{mix,LPF} = U(\omega) = \frac{D}{2}\left(-\frac{\pi}{2}\chi_0\omega_0(\omega-\omega_0)\frac{1}{\frac{1}{2}\delta\omega}\cos(\phi) - \frac{\pi}{2}\chi_0\omega_0\sin(\phi)\right)f(\omega)$$

$$= -\frac{D}{4}\chi_0\omega_0\frac{\frac{1}{2}\delta\omega}{(\omega-\omega_0)^2 + \left(\frac{1}{2}\delta\omega\right)^2}\left(\frac{(\omega-\omega_0)}{\frac{1}{2}\delta\omega}\cos(\phi) + \sin(\phi)\right).$$

(3. 21)

Finally, the amplitude terms can be understood as follows:

$$\chi_0 = \frac{n\gamma^2\hbar^2 S(S+1)\mu_0}{3k_B T},$$

(3. 22)

where n is the number of electrons transitioning per unit volume, S is the total spin and T is temperature;

$$D = \eta Q\sqrt{PZ},$$

(3. 23)

where η and Q are the filling factor and quality factor of the resonator respectively, and the input power and impedance of the signal to the resonator are given by P and Z. Hence, $\sqrt{PZ}$ is the amplitude of the input voltage. The amplitude of V_r is not mentioned as its contribution to the amplitude of $U(\omega)$ is negligible. Hence we can define

$$U_0 = \frac{D\chi_0}{2} = \frac{\eta Q\sqrt{PZ}}{2}\frac{n\gamma^2\hbar^2 S(S+1)\mu_0}{3k_B T}.$$

(3. 24)

Finally, the signal output from the mixer, excluding modulation, can be given as

$$U(\omega) = -U_0\frac{\omega_0}{2}\frac{\frac{1}{2}\delta\omega}{(\omega-\omega_0)^2 + \left(\frac{1}{2}\delta\omega\right)^2}\left(\frac{(\omega-\omega_0)}{\frac{1}{2}\delta\omega}\cos(\phi) + \sin(\phi)\right).$$

(3. 25)

In order to arrive at the signal, which is the final output of the spectrometer, the field modulation must be added, followed by the demodulation undertaken by the lock-in amplifier. Since the swept magnetic field is modulated, the equation must also be in the field domain in order to plot and fit to the data. The latter is easily achieved using the relation $\omega = \left|\frac{d\omega}{dB_0}\right|B_o$, resulting in

$$U(B_0) = -U_0 \frac{B_{0C}}{2} \frac{\frac{1}{2}\delta B_0}{(B_0 - B_{0C})^2 + \left(\frac{1}{2}\delta B_0\right)^2} \left(\frac{(B_0 - B_{0C})}{\frac{1}{2}\delta B_0} \cos(\phi) + \sin(\phi) \right),$$

Where $B_0 = |\boldsymbol{B}_0|$ and B_{0C} is the centre field value of the resonance.

The effect of the modulation of $\boldsymbol{B}_0$ by $\boldsymbol{B}_{mod}$ is an amplitude modulation of the signal, and the effect of demodulating this with the lock-in amplifier is that the measured signal output is an amplitude and phase modulated derivative of the true absorption signal. This is explained graphically in Figure 16 below, and results in the final equation for the output from the lock-in amplifier [55, 65]:

$$V_{LI}(B_0) = \frac{B_{mod}}{2} \frac{dU(B_0)}{dB_0} \cos(\theta)$$

$$= \frac{U_0}{2} \frac{B_{0C}}{2} B_{mod} \frac{\left((B_0 - B_{0C})^2 - \left(\frac{1}{2}\delta B_0\right)^2\right)\cos(\phi) + \delta B_0(B_0 - B_{0C})\sin(\phi)}{(B_0 - B_{0C})^2 + \left(\frac{1}{2}\delta B_0\right)^2}.$$

Here, θ is the phase dependency introduced by the lock-in amplifier. It does not appear in the second line because, as mentioned above, in practice, the phase is adjusted so that all of the signal appears in the X quadrature, hence we have $\theta = \cos(0) = 1$.
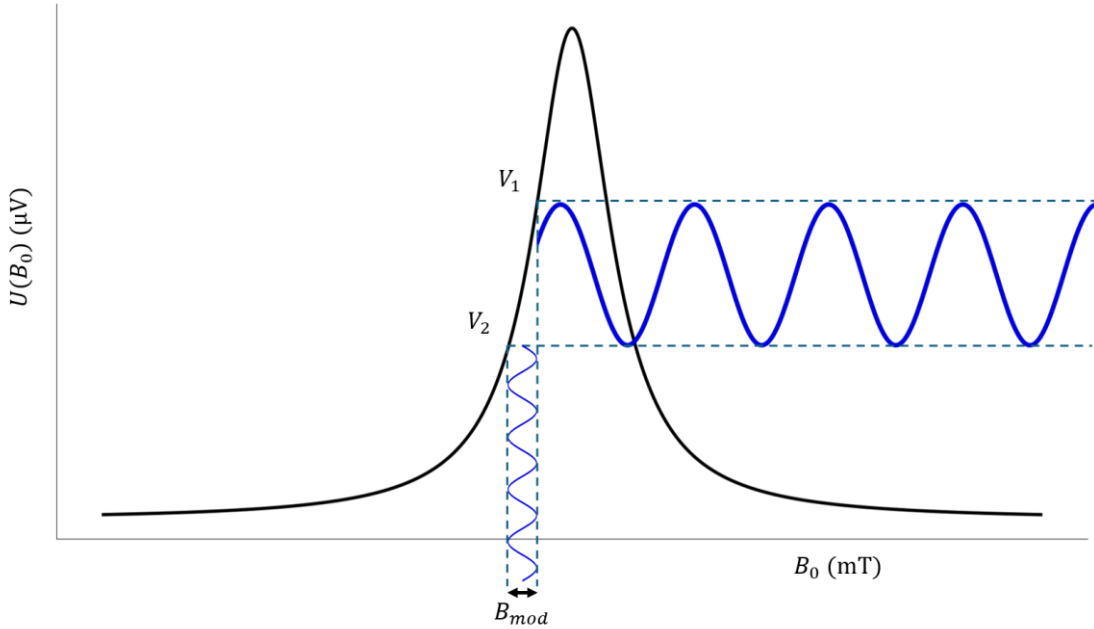
Figure 12. The effect of field modulation on the output signal. As $\boldsymbol{B}_0$ is swept, the field strength experienced by the spins oscillates with amplitude B_{mod}. Therefore, the output signal amplitude is proportional to the gradient of the absorption curve. When this is demodulated by the lock-in amplifier, it is the gradient which is being measured, resulting in an output which is a modified Lorentzian derivative, as in Figure 13 below.
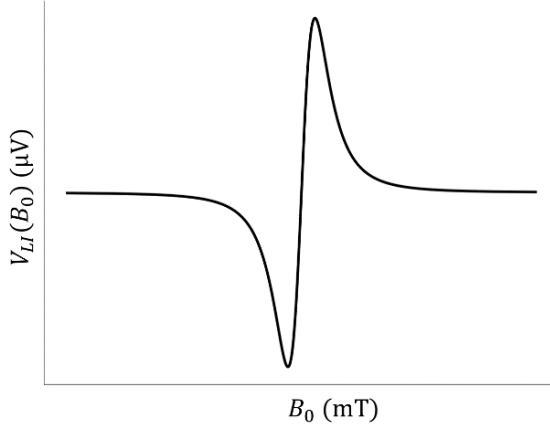
Figure 13. An example of the signal output from the lock-in amplifier, V_{LI}. Note that this has no phase modification.

It is evident from Figure 12 that if the modulation amplitude is too great, it will have the effect of broadening the measured line width due to the averaging of the absorption curve gradient. Other factors may also broaden the line and change the distribution, such as field inhomogeneities [65], Orbach processes affecting the spin-spin relaxation time [63], impurities in the sample and noise in the circuit around the resonant frequency. This manifests mathematically as the resonance line shape changing from a Lorentzian distribution to a Gaussian distribution. For this reason, it is important to have Gaussian versions of the equations (3.25 and 3.26), in order to enable analysis of the data.

These can be given by replacing equation (3.19) with a Gaussian distribution with $\delta\omega = 2\sqrt{2ln2}\sigma$ [55],

$$f(\omega) = \frac{1}{\sqrt{2\pi\sigma^2}}\exp\left(-\frac{(\omega - \omega_0)^2}{2\sigma^2}\right),$$

(3. 28)

such that the signal output from the mixer becomes

$$U_G(\omega) = -U_0\sqrt{\frac{\pi}{2}}\frac{\omega_0}{2\sigma}\left(\frac{\omega - \omega_0}{2\sqrt{2ln2}\sigma}\cos(\phi) + \sin(\phi)\right)\exp\left(-\frac{(\omega - \omega_0)^2}{2\sigma^2}\right).$$

(3. 29)

This can be converted to the field domain, as above, resulting in

$$U_G(B_0) = -U_0\sqrt{\frac{\pi}{2}}\frac{B_{0C}}{2\sigma}\left(\frac{B_0 - B_{0C}}{2\sqrt{2ln2}\sigma}\cos(\phi) + \sin(\phi)\right)\exp\left(-\frac{(B - B_{0C})^2}{2\sigma^2}\right).$$

(3. 30)

This is modified by the lock-in to produce a final output of

$$V_{LI,G}(B_0) = \frac{U_0}{2}\sqrt{\frac{\pi}{2}}\frac{B_{0C}}{2\sigma^3}B_{mod}\left(\frac{(B_0 - B_{0C})^2 - \sigma^2}{\sqrt{2ln2}\sigma}\cos(\phi)\right.$$
$$\left. + (B_0 - B_{0C})\sin(\phi)\right)\exp\left(-\frac{(B - B_{0C})^2}{2\sigma^2}\right).$$

(3. 31)

35

3.5 Turning the Spectrometer into a Clock

The spectrometer setup and signal derivation specified above form the oscillator, reference medium and detector from the atomic clock schematic in Figure 1. In order to create a functioning clock, the error correction signal and pulse per second signal extraction must be added. Figure 14 shows how this is done.
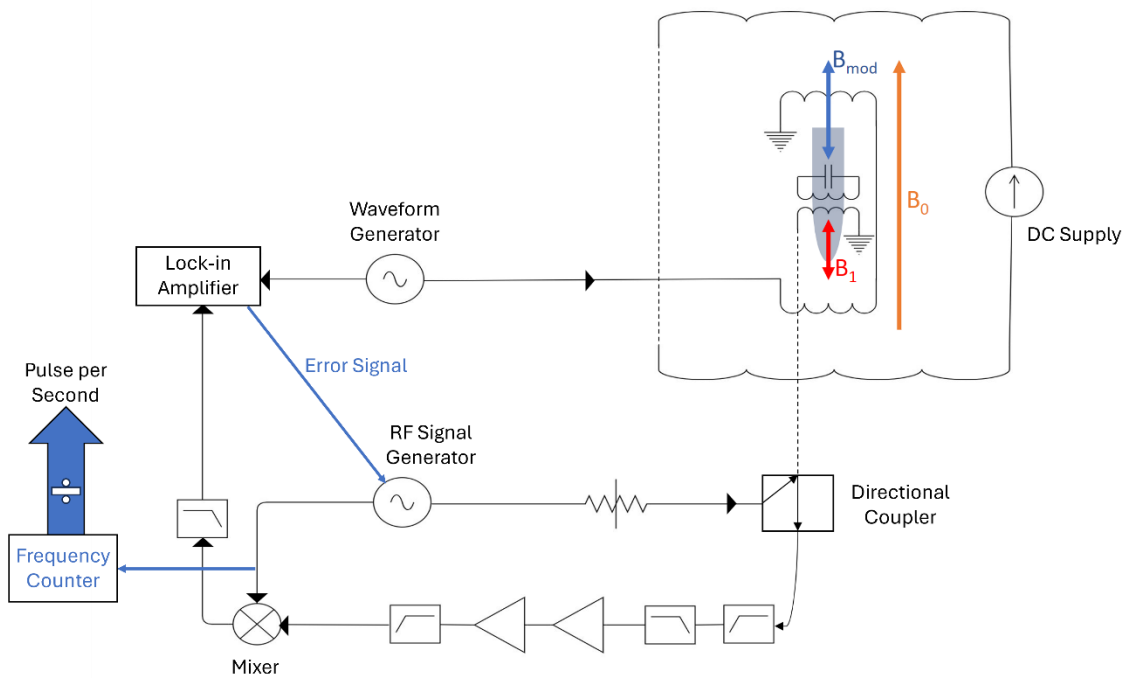
Figure 14. Circuit diagram of the spectrometer functioning as a clock. Modifications to the base diagram of Figure 10 are shown in blue.

The EPR spectrometer based clock is set to acquire a signal with the RF generator set to output the clock frequency and B_0 set to the clock field. The signal at this point should be zero, falling at the centre point of the Lorentzian derivative example in Figure 13, and the clock transition shown in Figure 21 below. The device is insensitive to field fluctuations at the clock frequency, and so drift is assumed to be due to fluctuations in frequency from the quartz oscillator based signal generator. If the frequency changes, a non-zero signal is generated since the absorption by the sample is reduced, giving rise to a change in the first derivative which forms the signal. This acquired signal is then coupled to the output of the lock-in amplifier and scaled such that when it is connected to the modulation input of the signal generator, it causes a perturbation to bring the RF output back to the clock frequency.

A frequency counter is connected to the output of the RF signal generator and is used to produce the frequency reference for the clock.

4. Objectives and Results

4.1 Spectrometer Optimisation

My first objective in the project was to optimise the spectrometer set-up in order to improve the signal to noise ratio (SNR) and accuracy of the field-swept data. The two major requirements in this regard were:

1. Demagnetisation
2. Resonator optimisation

4.1.1 Demagnetisation

It was found that the micrometer in use in the original set-up was magnetic. Since, in parallel mode, the micrometer is coaxial with all applied magnetic fields, this resulted in field-dependent distortions in the observed spectra. I designed new parts for the coupling loop platform control mechanism using Autodesk Inventor CAD, which enabled the use of a new brass differential screw, which I designed alongside an existing member of the team. Following printing and machining of the parts, I refitted three of the spectrometers in use and collected data to ensure success and quantify the improvement.
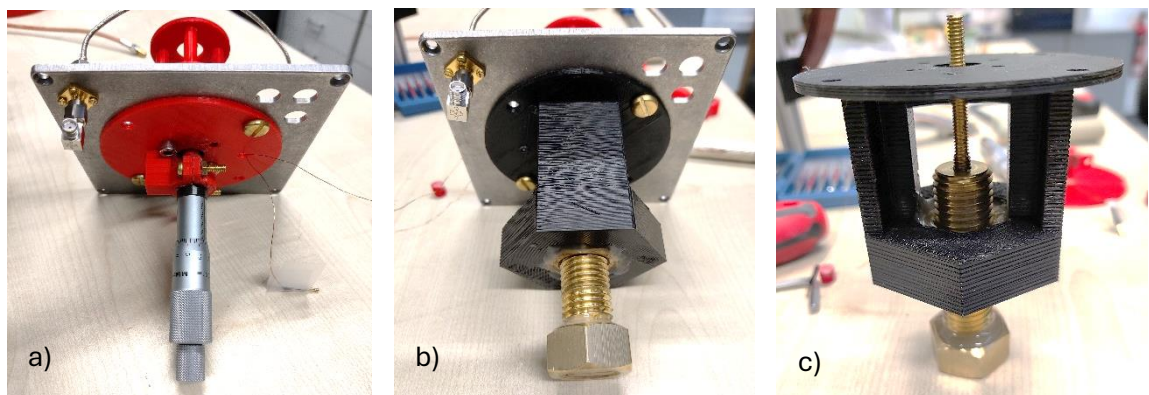
Figure 15. The old (a) and new (b & c) designs for loop-platform control, showing the micrometer and brass differential screw.
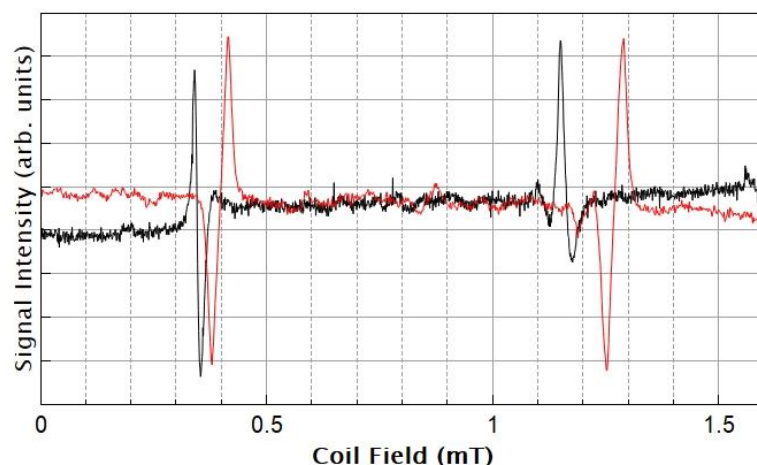
Figure 16. Identical sweeps at ~40.5 MHz with the micrometer (black) and brass differential screw (red). Differences of ~140 μT (upper peaks) and ~74 μT (lower peaks) can be observed, demonstrating the improvement.

4.1.2 Resonator Optimisation

The spectrometer originally used Harding's modified loop gap resonator (MLGR) design [49, 54] from the first spectrometer built to measure $^{15}N@C_{60}$ with respect to CSAC usage. This consists of a loop of copper tube of length ~10 mm, diameter ~10 mm, thickness ~0.5 mm, with a lengthwise cut slit, across which capacitors are soldered (see Figure 17).

Figure 17. Modified loop gap resonator. This is fixed to the outside of the vacuum tube containing the sample.

This can be modelled as a lumped-element RLC circuit, where the impedance of the bare resonator can be given by [49]:

$$Z = \left(i\omega C + \frac{1}{i\omega L + R} \right)^{-1},$$

(4. 1)

The natural resonant frequency can then be determined as the frequency for which the imaginary impedance tends to zero:

$$f_{nres} = \frac{1}{2\pi\sqrt{LC}} \left(1 - \frac{R^2 C}{L} \right),$$

(4. 2)

with the driven resonant frequency, as is the case in CW EPR, given by

$$f_{res} = \frac{1}{2\pi\sqrt{LC}}.$$

(4. 3)

Such resonators are also characterized by their quality factor (Q), which can be understood as the parametrisation of the energy dissipation in the resonator [49]:

$$Q \equiv 2\pi \frac{E_{stored}}{E_{diss,cyc}}.$$

(4. 4)

Here, the ratio is the energy stored in the resonator divided by the energy dissipated per cycle. In this thesis, I refer always to the loaded quality factor of the resonators, which

means the quality factor of the resonator including the additional losses to the inductive coupling to the transmission line and sample. This can be expressed as

$$Q = \frac{f}{\Delta f},$$

where Δf is the full width at half maximum of the electrical resonance frequency linewidth. Equation (4.5) shows that the linewidth is inversely proportional to the quality factor. This is important both for EPR measurements and for an atomic clock application, since a narrow linewidth will increase the SNR, use less power and result in a more responsive error correction signal in the case of frequency modulation. The increase in efficiency can be understood by noting that the magnitude of the oscillating drive field can be given by

$$B_1 = \sqrt{\frac{\mu_0 PQ}{2\pi V f}},$$

where P is the input power and V is the resonator volume. This shows that for a given input power and frequency, B_1 increases with the quality factor.

Whilst these modified LGRs produced a usable $\boldsymbol{B}_1$ field, they had a number of problems and disadvantages:

1. **Poor quality factor**. Q values ranging from 20 to 60 were the norm for our lab made MLGRs.
2. **Imprecise**. Difficult to manufacture to a precise frequency because only one parameter can be adjusted – the capacitance. This is further compounded by the fixed values of available capacitors and the difficulty of soldering delicate surface-mount components to a relatively large, thick mass of copper. Figure 17 shows the large amount of solder typically used, which adds resistance and capacitance unpredictably to the circuit.
3. **Inaccurate**. Drift in the resonant frequencies of the MLGRs was observed over time – see Table 3. The magnitude and unpredictability of the drift made them difficult to use for accurate data, particularly for the clock transition, whose frequency linewidth is very narrow.

LGR	f_{res} at manufacture	Max drift of f_{res} (3 months)
M1	39.90 MHz	2.75 MHz
L2	40.50 MHz	0.68 MHz
JL1	59.00 MHz	0.65 MHz
L4	38.80 MHz	0.05 MHz
L7	39.50 MHz	0.08 MHz
L5	38.40 MHz	0.04 MHz

Table 3. The original resonant frequencies of MLGRs and the maximum frequency change observed over a 3 month period. Note that even the smallest drift here (~40 kHz) would mean the clock transition would be unobtainable or highly compromised given its linewidth of (~100 kHz).

My first approaches to solving these problems yielded no significant benefits and consisted of the following:

1. The quality factor, Q, can also be written as

$$Q = \frac{1}{R}\sqrt{\frac{L}{C}},$$

   where R is resistance, L is inductance and C is capacitance. Hence, one way to improve it is to reduce the resistance. I tried using more capacitors, spread more evenly over the gap and each with a lower effective series resistance. This made small improvements in some cases but they were not repeatable.

2. Different approaches to soldering, including different types of solder (high and low temperature), masking fluid, and a conductive epoxy. Also different soldering iron heat levels and tips in an effort to minimise the solder and make it more consistent.

3. Cleaning and lacquering the MLGRs.

4. Measuring the variances of individual capacitors, solder and copper loops over time to try to identify the source of variance in order to model it and predict it.

5. Different models for the inductance, including as a single loop solenoid and Rinard & Eaton's formula for a standard LGR from [48], in order to shed light on the variance and aid precision. The MLGRs in the lab did not fit perfectly with any model.

My second approach was to make a solenoidal resonator. This form was suggested by Harding et al in 2017 [54] as a possible improvement, although he not been able to achieve good results when using them [49]. Harding used capacitive coupling, with a resulting source of imprecision in his experiment being these capacitors and their size. Hence, I designed the new resonator to be used with inductive coupling, with the standard surface mount capacitors in the same relative location with respect to the coupling loop as the LGRs. These are soldered across the two ends of the wire from which the coil is formed, which are bent out and parallel to the coil axis to create a gap (see Figure 18).

Figure 18. A solenoidal resonator. These are made to fit the dimensions of the vacuum tube containing the sample, and in such a way as to maximise the filling factor.

These have the advantages of being easier to solder due to the reduced mass of copper, and easier to make in the lab (from 0.9 mm bare copper wire) than the cut copper tubes of the MLGRs.

The precision is significantly increased due to their three adjustable parameters to change f_{res}: the inductance can be modified by changing the length and number of turns, and the capacitance can be adjusted in the same way as the MLGRs.

They are also simpler to model, with measurements of f_{res} agreeing closely with the standard formula for inductance of a solenoid substituted into equation (4.3):

$$f_{res} = \left(\frac{l}{4\pi^2 N^2 \mu_0 CA}\right)^{\frac{1}{2}},$$

<div align="right">(4. 8)</div>

where N is the number of turns, A is the cross-sectional area in the plane perpendicular to the axis and l is the length.

The initial design yielded a much-improved quality factor, which was gradually improved further, with testing over many devices demonstrating quality factors in the best solenoids approximately three times greater than MLGRs of the same frequency.

Figure 19. Quality factors for tested MLGRs and Solenoidal Resonators. Solenoids are shown in red, MLGRs in black.

This consistent improvement can be understood using equation (4.7) and considering the MLGR as a single-loop solenoid. Although there is slightly greater resistance in the solenoid due to the length of the copper wire, for a given frequency, the inductance is much greater and the capacitance much less than an MLGR. Since $Q \propto \sqrt{L/C}$, this yields a higher Q.

Finally, the precision was improved further by applying araldite to the capacitor and wire-end arrangement to allow controlled deformation post-manufacture. This is critical for the micro-adjustments to the length required to obtain the exact clock frequency.

The solenoidal resonators do not suffer from resonant frequency drift over time. This, coupled with the fact that the MLGRs do exhibit this, is interesting and remains to be understood. However, the scientific impetus of the project precluded further investigation

into the cause of this phenomenon since it was not observed in the better-performing solenoids.

4.1.3 Potential Improvements

Further improvements could be made to the design by precisely machine-winding (they are currently hand wound around a tube in the lab), or by laser cutting copper tube to the exact specifications. Additionally, whilst non-magnetic capacitors were sought for use, it was later discovered that the conducting plates contain a small amount of nickel, which is ferromagnetic and will result in a distortion in $\boldsymbol{B}_1$. Hence, truly non-magnetic capacitors would improve the homogeneity of the field produced by the resonator and hence results.

It would be possible to reduce the resistance of the solenoids (and hence further increase the quality factor) by winding Litz wire onto a thin substrate and fixing in place. The whole device could then be fit onto the vacuum tube. This would reduce resistance by minimising the skin effect. The skin depth of copper with a signal at 40 MHz is ~10.3 μm, whilst the solid copper wire used in these solenoids is 0.9 mm diameter, hence the current is restricted to a ~10.3 μm 'skin' around the outside. Litz wire (a braided set of individually insulated copper strands) of sufficient diameter would increase the total cross-sectional area through which the current could flow, hence reducing the resistance, R, since $R \propto \rho/A$, where ρ is the resistivity and A is the cross-sectional area.

However, such an arrangement would also slightly decrease the filling factor, η, by increasing the overall diameter of the solenoid. Since the signal strength is proportional to ηQ (see equation 3.23), it would be important to establish whether the increase in Q outweighs the decrease in η. Care would also be required in the choice of substrate to ensure it would not significantly affect the magnetic field.

4.2 Improve on Existing Published Data of the Clock Parabola

In 2017, Reuben Harding et al [54] published data showing the resonances of $^{15}N@C_{60}$ across the clock parabola (E_{67} from Figure 9). Harding's plot is reproduced below in Figure 20. Whilst the resonances are clear and in the expected locations, the SNR is poor and the clock transition itself is not visible except in the magnified inset. These data require improving upon for two reasons:

- The clock transition must be clear with high SNR and of the expected Lorentzian derivative shape in order to be useful in a clock application. This is because the error correction signal to be used for frequency feedback must be minimally noisy and highly accurate, and this signal is derived from the output of the lock-in amplifier.
- In order to constrain the hyperfine constant to a higher degree of precision, to enable better predictions of the molecular behaviour.

4.2.1 Data Acquisition

Harding et al were using MLGRs as mentioned above, with the associated problems. The low quality factor resulted in low SNR and the difficulty of precise resonant frequency in manufacture made it virtually impossible to accurately tune the resonator to the clock frequency.

Early sweep data from using the solenoids demonstrated a large improvement in both. In order to obtain the clock resonance, which has a very narrow frequency domain linewidth, it was necessary to araldite the capacitor area of the resonator and apply controlled deformation to the solenoid whilst installed on the sample tube. The resonant frequency is proportional to length, and so by slightly extending the coil, this frequency can be increased, and vice versa.

In addition to the improvements made using the solenoids, it was necessary to find and control multiple noise and interference sources. This involved examining the signal at multiple points in the circuit using an oscilloscope and spectrum analyser, and using the results to determine the sources of noise and solutions. Examples of note were:

- a sinusoidal interference pattern caused by an emission from an LED lamp control unit near the apparatus;
- a DC block on an adjacent spectrometer broadcasting the drive frequency from that apparatus;
- interference between the modulation frequencies of adjacent spectrometers, solved by setting each to a different prime number.

I also applied various different ground configurations to find the best combination and remove an apparent ground loop problem.

Following these optimisations, it was possible to recreate the plot of Harding et al by building appropriate frequency solenoidal resonators. The results are shown in Figure 21 below. In addition to the expected resonances, a series of doublets of much smaller curves can be seen ascending approximately linearly from ~1.15 mT to ~1.40 mT. This is from two perpendicular mode transitions, visible at small amplitude due to fringing of the

drive field at each end of the resonator and possibly a small degree of sample misalignment.
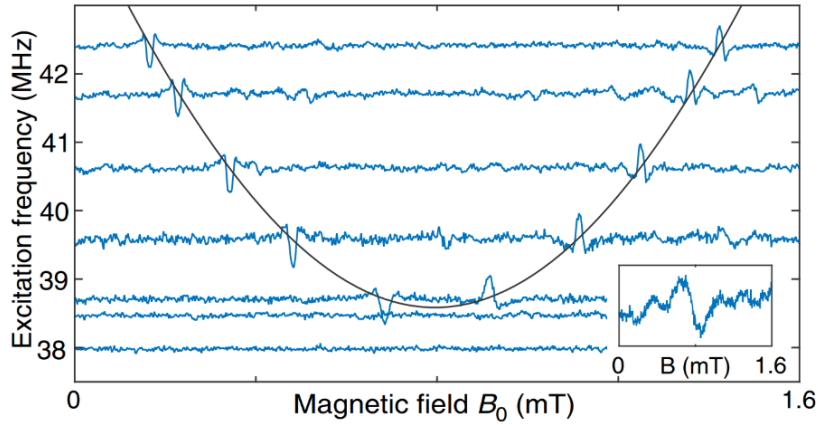
Figure 20. Clock parabola resonances from Harding et al, 2017 [54]. The inset is the clock transition from a sweep at 38.474 MHz, which traces just below the parabola. The parabola is a fit to the centre points of the resonance curves.
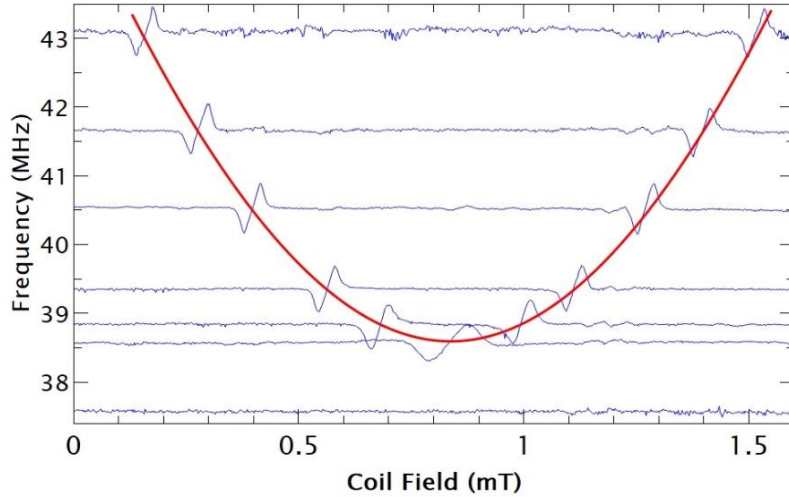
Figure 21. Clock parabola resonances using solenoidal resonators. The x-axis is the magnetic field magnitude generated by the Helmholtz coil pair, calculated using the coil constant. The hyperfine constant extracted from fitting is

$$\frac{A}{h} = -22.28 \pm 0.02 \text{ MHz.}$$

B_0 is given by $B_0 = \alpha B_{coil} + B_{offset}$ where α is a parameter to correct for random error such as sample misalignment, and B_{offset} is an environment field parameter. Fitting the data gives $\alpha = 0.996 \pm 0.006$ and $B_{offset} = -39.0 \pm 6 \text{ μT}$. This value of B_{offset} is approximately equal to the geomagnetic field magnitude in the lab in the axis of B_0. The extra noise in the upper sweep is explained below.

44

4.2.2 SNR and Allan Deviation

There is a clear improvement in SNR, defined as $\text{SNR} = S_0/\delta S$, where S_0 is the signal amplitude and δS is the root mean square noise per $\sqrt{\text{Hz}}$ bandwidth [54]. For the clock transition, Harding reports $\text{SNR}_{\text{clock}} \approx 2\ \sqrt{\text{Hz}}$, whereas the data in Figure 21 give $\text{SNR}_{\text{clock}} \approx 9.16\ \sqrt{\text{Hz}}$, using $S_0 \approx 867$ nV, and $\delta S \approx 94.6$ nV Hz$^{-\frac{1}{2}}$.

The SNR improvement translates into an improvement in the short term Allan deviation as follows. The transition quality factor is given as

$$Q_A = \frac{f_{clock}}{\delta f_{clock}},$$

<div align="right">(4. 9)</div>

where δf_{clock} is the frequency domain linewidth of the clock transition. The short term Allan deviation, defined as the fractional frequency stability over timescales, τ, for which the noise spectrum is approximately white [54], can then be given as

$$\sigma_y(\tau) \approx \frac{1}{\text{SNR} \times Q_A}\ \tau^{-\frac{1}{2}}.$$

<div align="right">(4. 10)</div>

Using an estimated value for the clock transition, Harding et al report $\sigma_y(\tau) \approx 1.3 \times 10^{-3}\ \tau^{-\frac{1}{2}}$.

Using the data from Figure 21, I extract $Q_A \approx 386$, giving

$$\sigma_y(\tau) \approx 2.8\ \times 10^{-4}\ \tau^{-\frac{1}{2}}.$$

This is an improvement of approximately one order of magnitude. Note that I have used $f_{clock} = 38.578550$ MHz and the estimated value for δf_{clock} from Harding et al of ~100 kHz because the fit to linewidth data involving the intrinsic dephasing time, T_2^*, used in [54] is not possible for the spectra in Figure 21 for reasons explained below. It is not possible to directly measure the frequency domain linewidth in this field-swept spectrometer setup.

4.2.3 Fitting, Hyperfine Constant and Linewidth Analysis

Despite this improvement, it was not possible to constrain the hyperfine constant to a higher precision than Harding et al. There appear to be three reasons for this:

- Line broadening due to over modulation;
- Possible broadening and line shape distortion due to the small amount of nickel in the capacitor conducting plates;
- The clock transition, although it appears as a single curve, is best fit using a double function, suggesting that the frequency used is slightly too high and is actually at a point just above the base of the parabola.

To obtain the parabola fit and extract the constants, the individual resonances were first fitted in order to find the centre points of the curves. I found that the Gaussian derivative signal equation (3.31) fit to the data more accurately than the expected Lorentzian

derivative (equation (3.27)). This indicates that broadening and possible distortion had taken place.

The transition parabola was then fitted to the resonance curve centre points using the equation for the curve describing the transition between the energy eigenvalues with respect to field (with scaling factors appropriate to the plot):

$$E_{67} = \frac{10^{-6}}{h}\Big[\big(g_{tot}\mu_B(\alpha B_{coil} + B_{offset})10^{-3}\big)^2 + 2g_{tot}\mu_B(\alpha B_{coil} + B_{offset})10^{-3} \times 10^6 A$$
$$+ 4(10^6 A)^2\Big]^{\frac{1}{2}}.$$

(4. 11)

Subsequent investigation into the effect of the modulation amplitude on the field domain linewidth revealed that these sweeps had been considerably overmodulated. A drive signal amplitude of 600 mV was applied to the modulation coils. However, as shown in Table 4, the line begins to broaden with modulation drive signal amplitude > ~40 mV.

Modulation Drive Signal Amplitude (mV)	B_{mod} (T)	Peak to Peak Linewidth (µT)	Best fit form of signal equation
10.00	1.39e-06	5.0	Amplitude too small
20.00	2.78e-06	5.0	Lorentzian
30.00	4.17e-06	5.0	Lorentzian
40.00	5.56e-06	5.0	Lorentzian
50.00	6.95e-06	6.0	Lorentzian
60.00	8.34e-06	6.0	Lorentzian
70.00	9.73e-06	6.0	Lorentzian
80.00	1.11e-05	7.0	Lorentzian
90.00	1.25e-05	7.0	Gaussian
100.0	1.39e-05	8.0	Lorentzian
110.0	1.53e-05	8.0	Gaussian
125.0	1.74e-05	8.0	Gaussian
150.0	2.09e-05	9.0	Gaussian
175.0	2.43e-05	11	Gaussian
200.0	2.78e-05	11	Gaussian
300.0	4.17e-05	17	Gaussian
400.0	5.56e-05	25	Gaussian
600.00	8.34e-05	38	Gaussian

Table 4. The effect of modulation amplitude on the signal linewidth. As expected, as the linewidth approaches its minimum value, the data fits better to the Lorentzian form, with one anomaly of note at 100 mV. Harding et al used approximately the equivalent of the 80 mV value from this setup, hence there is a large difference between the linewidths in Figures 20 and 21.

Further differences can be seen in analyses of the linewidth change with deviation from the clock field. In the field domain, the linewidth is expected to broaden for sweeps toward the clock transition - a phenomenon clearly apparent in the lower sweeps of Figure 21. The reverse is true for the frequency domain linewidth, δf, which is given by $\delta f = \left|\frac{df}{dB_0}\right| \delta B$.

Figure 22 shows the linewidth analysis from Harding et al [54], and Figure 23 shows the field domain linewidth analysis of the spectra in Figure 21. Both exclude the clock transition itself.
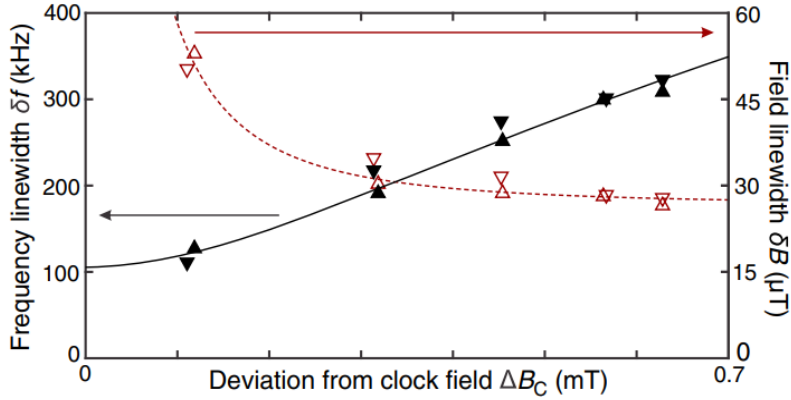
Figure 22. Linewidth analysis from Harding et al, 2017. [54]. Curves above and below the clock field are represented by up and down arrows respectively. The lines are fits to the field domain linewidths (dashed) and frequency domain linewidths (solid).
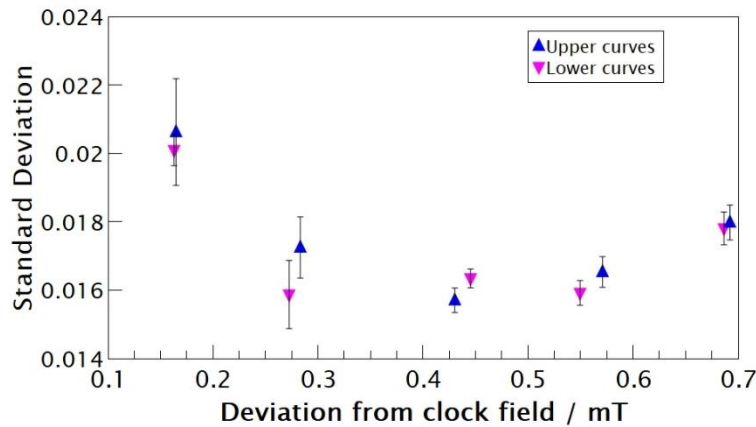
Figure 23. Linewidth analysis of the spectra in Figure 21. The points are the standard deviations of the Gaussian fits, with the same arrow convention as Harding et al. The frequency domain linewidths were not calculated since it was evident that the data did not fit the expected pattern. Error bars show the statistical uncertainty in the standard deviations arising from the fits.

Two main differences between the two datasets are evident. Firstly, the linewidths of the upper and lower curves are not as closely aligned in my data as in that of Harding et al. The Gaussian fit indicates that the data is less accurate, with greater randomness, and whilst the major factor in this appears to be the overmodulation, it is possible that another, undetected factor is at play. Since there isn't a pattern of either upper or lower curves showing the greater linewidth for the same frequency, this precludes a field dependent phenomenon.

The second difference is an aberration in the expected pattern of reduction of field domain linewidth with deviation from clock field. The two upper frequency sweeps in my data show curves with a greater linewidth, than sweeps lower in frequency. This is the opposite of what is expected and a possible cause is implicated as follows.

During the period of data acquisition, I changed the cable length between the signal generator and coupling loop in order to keep the phase of the signal the same across all sweeps. This was necessary because the change in wavelength alters the phase of the

47

signal at the demodulation point. It was initially impossible to acquire the upper two sweeps (~41.7 MHz and ~43.1 MHz) without significantly higher noise than the others. Eventually, I found that the position, shape and length of the cable between the attenuator and coupling loop had a large effect on noise at particular driving frequencies. I was able to solve this for the ~41.7 MHz sweep but did not have time to do so for the ~43.1 MHz sweep. I was not able to identify the exact reason for this problem, but it appears to be due to the cable acting as an antenna. The solution for the ~41.7 MHz sweep involved using a longer cable arranged in an S shape instead of a shorter, straighter cable. Similar issues were found by altering cable lengths and shapes elsewhere in the circuit.

It is possible that the extra noise in these sweeps has further broadened the line and possibly affected the shape. It would be possible to continue to experiment with cable and component arrangements and to attempt to find the source of the interference, however the scientific goals for the project were satisfied by these data and it was necessary to move on to further objectives.

4.2.4 Potential Improvements

The following changes could be considered in order to make improvements to these data:

- Reducing the modulation drive signal amplitude to ~40 mV would result in an accurate linewidth and more accurate fitting. It would, however, also reduce the signal amplitude (see Table 5 below), thus reducing SNR. This would put greater requirement on further noise reduction with regard to a CSAC application.
- Further micro-adjustments could be applied to the resonator to increase the accuracy of the clock frequency, measurable through multiple sweeps and finding the best fit of the expected single Lorentzian form.
- This experiment was undertaken in an electromagnetically noisy lab environment. Using the set up in a more isolated environment and/or with magnetic shielding should improve SNR. Similarly, further into the CSAC application development pathway, the integration of instrumentation will reduce the propensity for cables and components to act as antennas and otherwise attract external interference, thus increasing SNR.
- The sample volume and resonator could be adjusted to ensure the end planes of the resonator are exactly parallel to the ends of the cylindrical sample volume. This would reduce field fringing effects and remove the perpendicular transition faintly observed in Figure 21.

Whilst the clock transition is significantly improved in amplitude and SNR over previous attempts, there was still 40 s of averaging per point used, with a lock-in time constant of 10 s. It would not be possible to use this amount of averaging in a functioning atomic clock, and so further noise reduction is still required.

Modulation Drive Signal Amplitude (mV)	Peak to Peak Linewidth (µT)	Signal Amplitude (µV)
10.00	5.0	0.18
20.00	5.0	0.35
30.00	5.0	0.45
40.00	5.0	0.51
50.00	6.0	0.76
60.00	6.0	0.84
70.00	6.0	0.94
80.00	7.0	1.00
90.00	7.0	1.04
100.0	8.0	1.04
110.0	8.0	1.08
125.0	8.0	1.16
150.0	9.0	1.16
175.0	11	1.20
200.0	11	1.12
300.0	17	1.03
400.0	25	1.08

Table 5. Effect of modulation amplitude on linewidth and signal amplitude.

4.3 Low and Zero Field Transition Mapping

The next objective for this thesis was to record resonances at low and zero field, including into the negative field regime, where $\boldsymbol{B}_0 = -B_0\hat{z}$. Due to the reversal of the sign of the magnetic field, plotting the transition frequencies to either side of zero field gives a plot with a line of reflection at $B_0 = 0$, as can be seen in Figure 24 below.
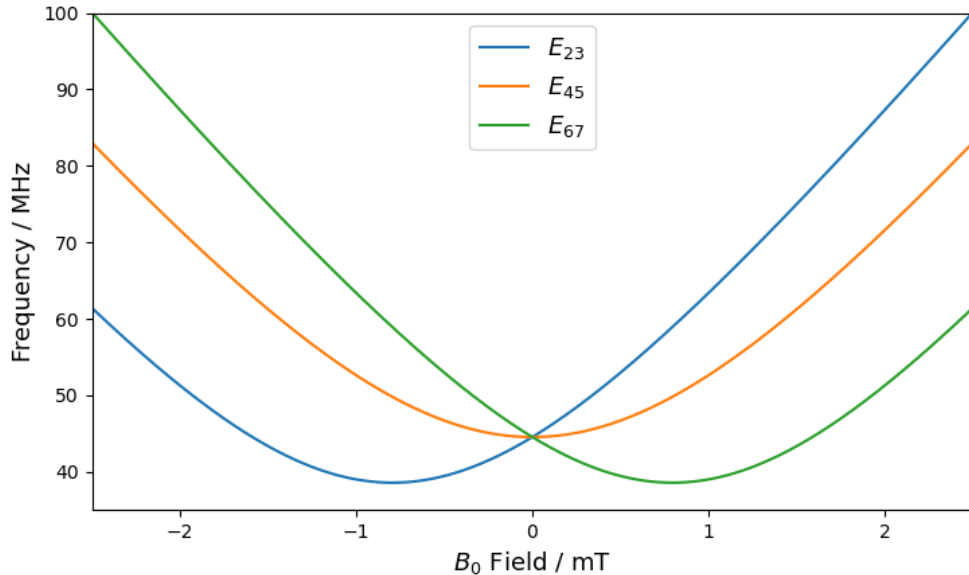
Figure 24. Transition frequencies at either side of zero magnetic field.

There were three aims in undertaking this task:

1. Establish a more accurate constraint on the hyperfine constant.
2. Explore the potential of sweeping multiple frequencies with the same resonator at a single $\boldsymbol{B}_0$ value.
3. Establish the limit of deviation from the electrical resonant frequency of the resonator at which it is still possible to obtain a resonance signal.

4.3.1 Reconfiguring the Spectrometer

Since the magnitude of B_0 being used would be < 50 μT, the geomagnetic field, and potentially other environmental fields, would have a large effect on the measurements, causing significant field offset. To reduce this as much as possible, the spectrometer apparatus, including coil set, frame, inner cage and sample (but excluding filters, amplification and instruments) was placed into a large Mu-metal box – see Figure 25.

Using a mobile phone magnetometer at the position of the box in the lab, at the time of the experiment, the total environmental field magnitude was measured at ~49 μT outside the box and ~1.8 μT inside the box. Mu-metal has a high magnetic permeability, and so causes the extraneous magnetic field lines to 'flow' within the cage material itself rather than be transmitted to the interior volume.

Figure 25. The Mu-metal cage into which the apparatus was placed. The holes are from the removal of BNC and serial connectors, two of which can still be seen in place.

Once in the cage, the grounding configuration of the spectrometer, and of the box itself, had to be re-optimised. I found that connecting cables to the box via BNC connectors to pass through resulted in ground loops and excessive noise. I removed these connectors so that the cables could pass through insulated, and secured them in place. Whilst this likely had a slight negative effect on the shielding (below the precision level of my magnetometer, so I could not confirm), it was the best compromise. The box itself was left ungrounded as this yielded the best results.

The resonator coupling regime also required alteration. The high quality factor of the solenoidal resonators means their linewidth is narrow when critically coupled. In order to attempt to measure multiple transitions with the same resonator, it was necessary to have as broad a linewidth as possible, so that the resonances could be measured sufficiently far from the point toward zero field at which they become indistinct.

Following several initial experiments, I found that maximal overcoupling would be necessary – this has the coupling loop positioned central to the length of the resonator, which is made possible by the coupling loop's larger diameter. This gave an electrical loss of ~4.9 dB at the electrical resonant frequency and ~1.9 dB at ±800 kHz from f_{res}.

4.3.2 Data Acquisition

The data were acquired in the same way as the clock parabola data but plotted in a 2D intensity map. The results are shown in Figure 26 below, and were obtained with a single resonator with $f_{res} = 44.52$ MHz. It took approximately 4 weeks to run all the sweeps, a large portion of which coincided with the Christmas break and a quiet time in the laboratory, resulting in lower noise and disturbance. Averaging per point was 30 s, with the lock-in time constant set to 7.5 s with filter order 8.

The initial data were significantly better than expected, so I extended the plot to higher frequencies by running additional sweeps to explore the limit of the resonator. In order to do this, I also increased the width of the sweep, which necessitated running additional sweeps at the original frequencies to extend each to the same field values as the new ones. This is visible on the plot at 0.28 mT, from 45.05 to 45.20 MHz, where the background offset has changed, and does not affect the resonances. The original set of

sweeps ran from 43.80 to 45.20 MHz. Even with the extension to 45.60 MHz, the limit of the single resonator to obtain spin resonance signals was not reached. Time constraints precluded further measurement.

A phase change can be observed across all transition curves at 44.85 MHz. The sweeps were set to run automatically, and so the cable lengths were not adjusted as they were in the clock parabola measurements, nor was any other phase adjustment applied. Thus, this phase change is partly a natural consequence of the changing wavelength, however, it is too sudden to be attributed only to that. The rate of change is more easily observed in Figure 27, which shows the individual spectra per frequency, with fits to each resonance. The phase change occurs simultaneously with a change in background offset, the reason for which is that this sweep coincided with greater activity in the department after Christmas. It is likely that this was an environmental issue: in the optimisation process, the ground was shown to affect the offset in the lock-in output signal - with more active devices connected to the ground, this changes slightly. However, the mechanism by which this would cause a phase change in the signal is unclear, and its coincident timing should not be interpreted as a definite cause. Further work should be undertaken to better understand this phenomenon, beginning by attempting to replicate it.
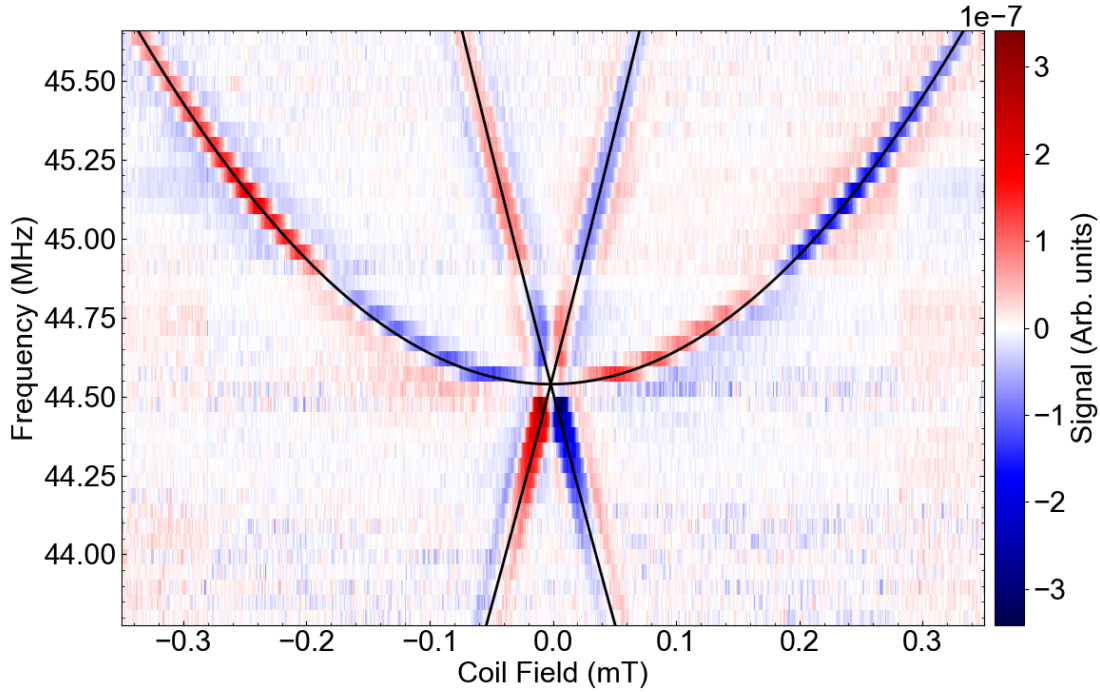

Figure 26. Low and zero field transitions of $^{15}N@C_{60}$. The black lines are fits to the data using the transition curve equations derived from the energy eigenvalues (see below).
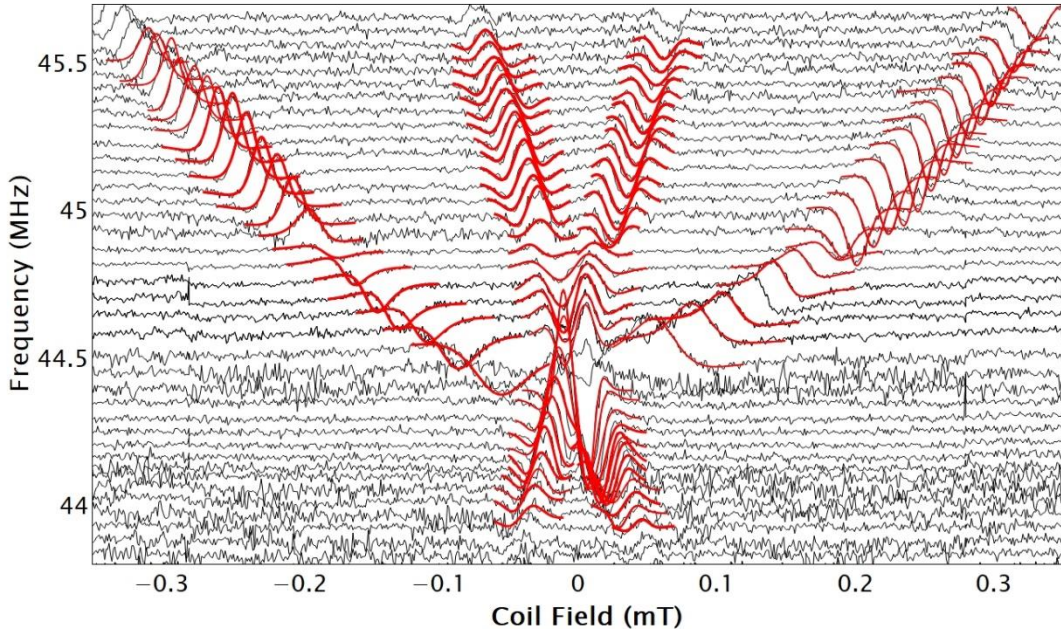
Figure 27. Low field spectra showing individual sweeps with fits to the resonances.

4.3.3 Fitting and Analysis

The Lorentzian or Gaussian equations (3.27, 3.31) were used to fit to the data for each resonance independently. Those on the curve E_{45} fit well to the expected Lorentzian form, but those on E_{67} and E_{23} fit better to Gaussians. The reason for this appears, again, to be due to modulation amplitude. A modulation drive signal amplitude of 300 mV was used despite the findings in the previous section, as it was necessary in order to increase the signal amplitude to the required amount in the overcoupled regime. The reason this has affected the two central curves more greatly is due to their steeper gradient and narrower field domain linewidth. Referring to Figure 12, the effect of overmodulating will tend to 'smear out' the sharper Lorentzian curve into a broader Gaussian distribution.

Despite this effect, the centre point of each distribution should not be greatly affected, and it was therefore hoped that the very large number of data points available for curve fitting would still enable an accurate hyperfine extraction. Toward the point where the three transition curves meet, most notably on the E_{23} and E_{67} curves, there were several resonances to which a satisfactory fit was not possible, even using combinations of double functions. This seems to be due to interference between the signals from each, and possibly limitations of the fitting software, QTI Plot in this case. A total of 30 centre points of resonance signal curves out of a possible total of 120 were excluded for this reason.

The E_{67} curve was fitted with equation (4.11), whilst E_{23} and E_{45} were fitted with equations corresponding to their eigenvalues as follows:

$$E_{23} = \frac{10^{-6}}{h} \Big[\big(g_{tot}\mu_B(\alpha B_{coil} + B_{offset})10^{-3}\big)^2 - 2g_{tot}\mu_B(\alpha B_{coil} + B_{offset})10^{-3} \times 10^6 A$$
$$+ 4(10^6 A)^2 \Big]^{\frac{1}{2}};$$

<div align="right">(4. 12)</div>

$$E_{45} = \frac{10^{-6}}{h} \Big[\big(g_{tot}\mu_B(\alpha B_{coil} + B_{offset})10^{-3}\big)^2 + 4(10^6 A)^2 \Big]^{\frac{1}{2}}.$$

<div align="right">(4. 13)</div>

The curve fitting was undertaken in Python by applying the Levenberg–Marquardt algorithm simultaneously across the three curves, using shared parameters to obtain the most accurate estimates for the constants. This yielded the following results:

$$\frac{A}{h} = -22.26950 \pm 0.00003 \text{ MHz},$$

$$\alpha = 1.07043 \pm 0.00008,$$

$$B_{offset} = 1.859 \pm 0.004 \text{ μT}.$$

The field offset is as expected, and the correction parameter, α, is close to 1 and reasonable given the hand-wound resonator and placement of the sample in the apparatus. Considering this statistical uncertainty alone yields a value for the hyperfine constant of the highest precision in the literature, to the best of my knowledge, and one which falls within existing values. However, further experiments would be required in order to better understand sources of systematic error which may not be properly represented in this value. For example, the Gaussian fits applied to the E_{23} and E_{45} curves include some randomness, and it may not be true that the centre points are unaffected – the additional averaging of the curve due to overmodulation may shift the centre in favour of the side of the transition curve with the steeper gradient.

The value for A/h stated here differs from that of Harding et al [54] by 0.0075, despite a similar spectrometer setup and techniques. This can be understood in terms of the temperature dependence, known from experiments with $^{14}N@C_{60}$ [54] to be

$$\frac{1}{A}\left(\frac{dA}{dT}\right) = 89 \text{ ppm K}^{-1}.$$

<div align="right">(4. 14)</div>

This yields $dA/dT \approx 0.0020 \text{ K}^{-1}$. The temperature in the laboratory in which my experiment was conducted is frequently between 25 and 28°C due to adjacent experiments and so a temperature difference of 3 to 4°C from that of Harding et al seems reasonable.

It can be observed from Figure 26 that it is possible to successfully sweep at least two frequencies with a single resonator without altering the coupling or resonant frequency of the device.

Aims 1 and 2 of this objective are thus satisfied. The absolute limit of resonance frequency deviation for transition stimulation for a single resonator remains to be determined.

4.3.4 Potential Improvements

Some of the suggested improvements from the clock parabola sweeps were included in this experiment to apparently positive effect. The apparatus was more greatly isolated, the resonator was sized correctly to sample volume and the modulation amplitude was reduced. However, in order to achieve sufficient signal amplitude in the overcoupled regime, the sweeps were still overmodulated, as evident in the Gaussian fits. To increase accuracy and confidence in the extracted hyperfine constant value, the sweeps could be individually repeated with a critically coupled resonator and a modulation amplitude of ~40 mV. This would allow more precise fits with the expected modified Lorentzian function.

However, it would take a long time to acquire the data in this way. An alternative might be to derive a more sophisticated fitting equation which includes parameters to account for the effect of the overmodulation, and combine this with the modified Lorentzian. The predictive accuracy of such a function would still require experimental verification.

Whilst the phase change at 44.85 MHz does not appear to affect the centre point of the curve, work should be undertaken to better understand it. Replication should be the first step, followed by finer frequency adjustments to better observe the change. Different cable lengths could then be used to determine if the phase changes according to the calculated wavelength of the signal in coaxial cable. Differences in phase changes at the resonator related to the overcoupled regime compared to the critically coupled regime could also be investigated.

Further improvement could be made by a still greater degree of isolation and more integrated electronics. Greater sensitivity and SNR might be possible using cryogenic amplifiers whilst keeping the sample at room temperature [66]. Greater averaging time with either a lower lock-in time constant or greater pause between points might improve the resolution of the central resonance curves, enabling more data points to be used for transition curve fitting.

4.4 Simultaneous Detection of Two Transitions

Whilst the clock transition between energy levels 6 and 7 provides a field-insensitive resonance, another option is to add a field stabilisation feedback mechanism, in addition to the proposed frequency feedback to achieve better overall environmental resilience. In order to achieve this efficiently in a CSAC device, it is optimal to measure two resonances simultaneously with a single resonator at the same B_0 value, with two resulting signals. One signal can then be used as the clock frequency reference and to provide the frequency error correction, whilst the other is used for field error correction.

4.4.1 Initial Data Acquisition

The data in objective 3 provided the basis for finding the optimal field and frequency values. In order to maximise the signal strength for each transition, maximum proximity in frequency is desirable whilst minimising any of the interference around the zero field point. The positive branches of curves E_{23} and E_{45} were the obvious choice, but an additional complicating factor is the changing gradient of E_{45}. This approaches zero toward zero field, with a consequently broadening field domain line width.

I undertook an initial set of sweeps with single frequency using the resonator in the overcoupled regime as for objective 3. In each, the resonator was adjusted to have a resonant frequency equidistant in value between the two target frequencies for the sweeps. This was established using the VNA, whilst ensuring that the power loss from the coupling loop to the resonator was approximately equal at the two target frequencies. This was achievable to 2 significant figures at -2.8 dB.

The best combined result from these data is shown in Figure 28. This established a working optimal field value with which to proceed to the next step of the experiment.
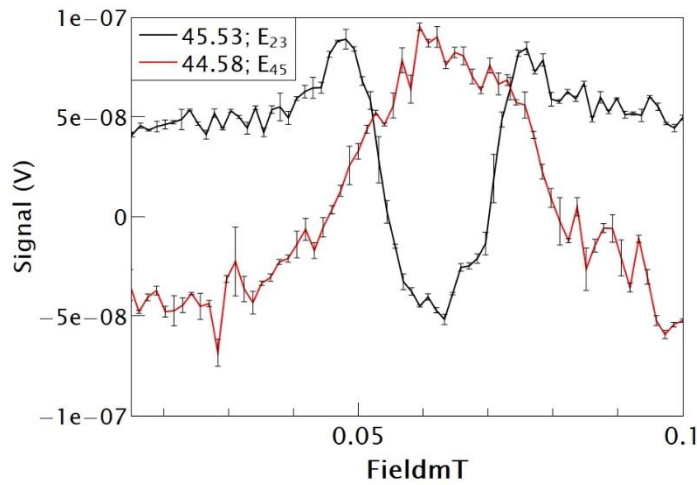

Figure 28. Two sweeps undertaken separately demonstrating coordination in the resonance peaks at a single value in field. It was not necessary at this point to precisely align the centre points or phases, because the changes in the spectrometer instrumentation would likely result in small changes necessitating final realignment.

4.4.2 Spectrometer Reconfiguration and Troubleshooting

In order to illuminate the sample with two frequencies simultaneously, it was necessary to reconfigure the instrumentation to allow a two tone input. During the process of measurement optimisation, I made a large number of changes to the setup whilst attempting to obtain usable signals. I will summarise the major and important changes, along with their reasoning, in this section.

It was initially necessary to introduce a second RF signal generator (RF2), with a second homodyne mixing arrangement. The output signals from RF1 and RF2 were connected via a combiner before being connected to the variable attenuator as a combined signal. Both tones then passed through the coupling loop, filters and amplifiers and then into a splitter which passed the signal to two separate mixers. The mixers were singly connected to the RF generators in two homodyne arrangements. A multi-oscillator lock-in amplifier was used to demodulate both mixer output signals separately (using the same modulation frequency source). This utilised the signal input and first auxiliary input ports of the lock-in.

Following power, attenuation and amplifier gain adjustments (including experiments with three different amplifiers) throughout the circuit in order to optimise the signal, I found that the auxiliary input on the lock-in had insufficient sensitivity adjustment to record a usable signal, and also that the signal from one tone was extremely noisy when both tones were in the circuit. This latter effect was component independent.

Switching to two lock-ins, synchronised using the Zurich Instruments MDS protocol, enabled the successful recording of both signals, but still with significant noise ($SNR < 2$, compared with $SNR > 7$ for single tone). In attempting to diagnose the problem, running a wider sweep revealed that both sets of resonances (those expected at each frequency) were visible on both signal branches.
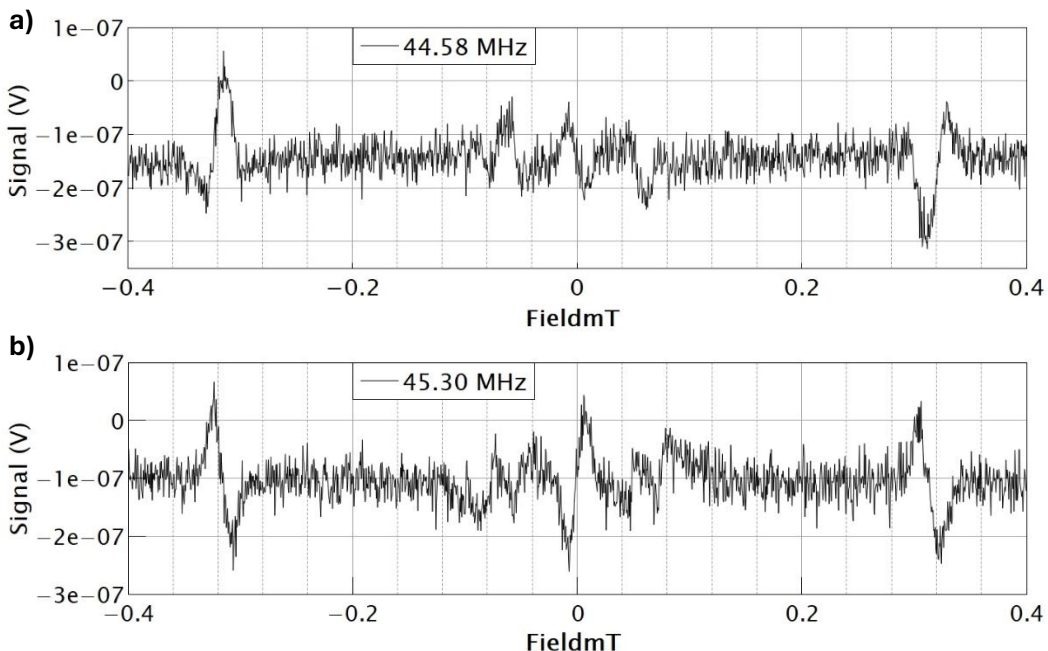

Figure 29. Two sweeps at different frequencies, both showing resonances which should only appear on the other.

On review of such effects in the literature, it appeared that the noise and duplicated resonance phenomenon could be products of intermodulation distortion (IMD) [67] and cross modulation [68] respectively. IMD is caused by non-linearity in signal processing components, particularly amplifiers, and produces additional components to the original frequencies at both the sums and differences of those frequencies, and the sums and differences of their harmonics. It is more problematic than harmonic distortion, particularly for the purpose here, because the third order intermodulation products produce additional signal components very close to the original frequencies. This is more pronounced with original frequencies close in magnitude, because original frequencies f_1 and f_2 produce third order IMD products at $2f_1 - f_2$ and $2f_2 - f_1$. This is a particular problem because these components cannot easily be removed using band pass filters.

Cross modulation is a related phenomenon in which the amplitude modulation in one signal is transferred to another. Commonly, it is considered that an undesired AM signal affects a desired signal, however, in this case, both signals are desired and so neither can be eliminated to resolve the problem. Whether or not cross modulation is an issue in this setup remains unresolved at time of writing. Complexity arises due to the consideration of the nature of the signals. At output from the signal generators, they are not amplitude modulated, however, on resonance, and close to it at either side, they become so due to the field modulation B_{mod}, which moves the spin system in and out of absorption, thus modulating the power of the reflected signal from the resonator.
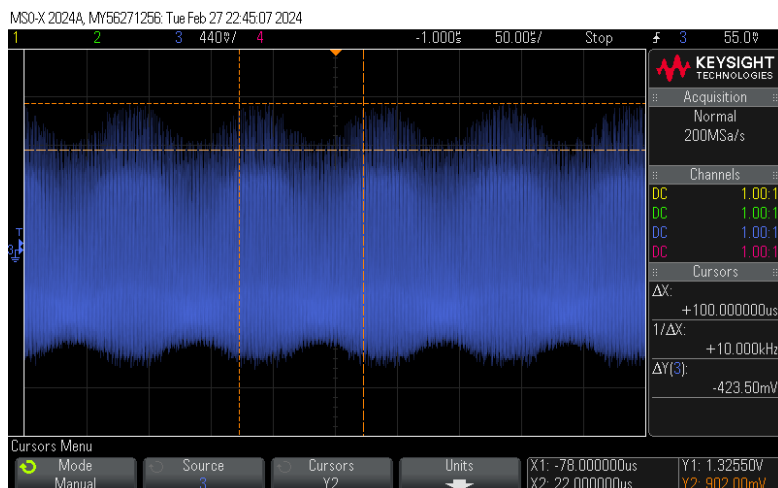
Figure 30. Oscilloscope trace showing modulation of the post-mixed RF1 signal by the amplitude modulation of the output from RF2.

In order to test this possibility, I set the output of RF2 to be amplitude modulated, kept the system off resonance, and measured the output of the mixer connected to RF1. The amplitude modulation was observable using an oscilloscope, as shown in Figure 30. However, the amplitude modulation used was greater than that which would be caused by the spin response to B_{mod}, and the effect smaller than that which appears in the lock-in output signal, wherein the resonances appear at the same amplitude on each trace. This suggests that cross modulation is a contributory factor but not the entirety of the problem.

In an effort to combat these effects, and to test the degree to which each might be applicable, I added an extra coupling loop to the internal platform set up, and completely separated the circuits from each RF signal generator. This caused all of the signal to disappear almost entirely, a phenomenon which proved to be due to inductive coupling

between the coupling loops and resonator. A transmission test undertaken with the VNA demonstrated frequency dependent transmission of power from one coupling loop to the other, centred on the resonant frequency of the solenoid. Initially, the coupling loops were maximally separated from each other at either end of the resonator, in order to try to minimise mutual coupling between the two loops. Following the transmission test, I fixed the two coupling loops adjacent to each other, both as close to the midpoint of the solenoid length as possible to ensure maximal overcoupling. An example of the data produced in this regime is shown in Figure 31.
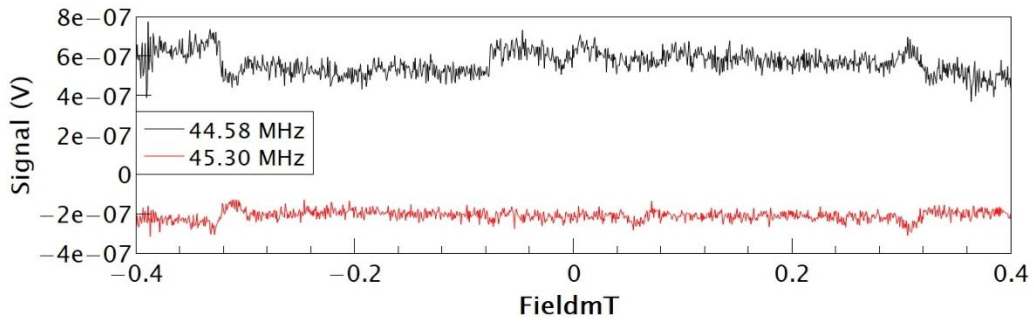

Figure 31. Sweeps of each frequency with separate circuits for each and with two coupling loops coaxially adjacent.

The data in Figure 31 is of insufficient quality to draw firm conclusions, however it appears to tentatively confirm that cross modulation is just a contributory factor. Only the outer resonances ($\pm\sim0.3$ mT) are visible on both sweeps, and the central resonance around the zero of field appears only at 44.58 MHz, which is as it should be. So the effect has been reduced but not eliminated by separating the electrical circuits.

4.4.3 Suggestions for Continuation of the Work

Unfortunately, time constraint precluded further progress on this objective, however, the above provides a basis upon which the work can be continued going forward. Rather than suggest improvements, I will therefore discuss ideas for the next steps.

Further work comparing the double coupling loop arrangement with the single coupling loop set up would be useful to determine the degree to which IMD and cross modulation are the cause of noise and spurious signals. This could be quantified by undertaking sweeps with a large amount of averaging and comparing the data. Furthermore, the third order IMD products increase non-linearly with input signal power – for 1 dB increase in input, third order IMD products can increase by up to 3 dB. This can be measured at each step in the circuit using a spectrum analyser, to find both the source(s) and magnitude of the problem.

IMD is caused by non-linearity in electronic components, particularly amplifiers, where non-linearity means that the output signal power does not increase linearly with input signal power. The amplifiers used in this circuit are approximately linear at the frequencies used here, however, devices with a better linearity rating are available and could be used.

The data in Figure 31 is inconclusive and efforts should be made to get better data from this setup. However it suggests that there is a component of the spurious signal

appearance that is not related to IMD, nor to any direct physical connection of the circuits. This leaves mutual inductance, instrumental problems and broadcast/antenna effects in components. As in the cases of the DC block broadcasting a signal, and the cable picking up a signal, both mentioned above, this can be tested using an oscilloscope and spectrum analyser at each point in the circuit, all with various combinations of instruments switched on and off and with outputs on or dormant.

Similar tests with an oscilloscope to that undertaken in Figure 30 could be used with the double coupling loop setup to examine the degree to which amplitude modulation, or other effects, are transmitted from one circuit to the other via the mutual inductance of the coupling loops and resonator.

The observed signal is due to reflection at the coupling loop due to impedance mismatch with the resonator. This is due to the change in inductance, and thus impedance, of the resonator by the magnetic susceptibility of the sample, as per equation 3.15. If the physical inductance of the resonator is changed due to a resonance induced by one input frequency, this will cause an impedance mismatch resulting in reflection of both input frequencies and hence observable 'resonances' in both circuits and output signals.

The induction perturbation due to χ is generally considered to be a frequency-dependent phenomenon and so it is not clear whether this could be the case, although the data suggest it is possible. It might be possible to test this by measuring the strength of inductive coupling of one coupling loop at a range of frequencies, using a VNA, whilst running the spectrometer as normal using the other coupling loop and frequency. However, since this would take place in a live experiment with multiple coaxial coils and associated mutual inductances (a small amount of coupling also takes place with the modulation coils, demonstrable as an observable DC offset in the output traces), extreme care would need to be taken to separate out all of the various effects.

An alternative approach might be to design and use a resonator with a double resonance frequency, such as that used in an LLC resonance converter [69]. This has two inductors, one in series and one in parallel to the capacitor, generating two resonant frequencies:

$$f_{series} = \frac{1}{2\pi\sqrt{L_s C}},$$
$$f_{parallel} = \frac{1}{2\pi\sqrt{(L_s + L_p)C}}.$$

<div align="right">(4. 15)</div>

This would have the advantage that a suitably tuned device could be critically coupled, rather than the overcoupled regime used above, thereby transmitting much more of the power to the sample and improving the SNR. However, the construction would be complex given that the inductors must be coaxial, which may lead to further problems due to mutual inductance.

5. Overall Conclusions and Outlook

The purpose of the work in this thesis falls into three main categories:

1. Generate technological improvements to the proof of concept spectrometer setup which can potentially later be used as the basis for a chip scale atomic clock.
2. Add to current knowledge of the behaviour of ^{15}N@C$_{60}$ at low and zero field and improve on the precision of the hyperfine constant, providing experimental data to support theory.
3. Develop the proof of concept of a method of field stabilisation which could be used in an alternative approach to the clock set up.

The demagnetisation, noise reduction and resonator optimisation of the first objective contribute to point 1, both in the self-evident improvements of signal accuracy and quality factor, and also in the clock parabola sweeps of the second objective. Significant improvements have been achieved in both SNR and short term ADEV, demonstrated in the data, in particular of the clock transition itself. There is also room for further improvement in these areas, as specified in the sections above.

The low field parallel mode transition spectra of ^{15}N@C$_{60}$ have been successfully mapped, yielding a value for the hyperfine constant of high precision, and demonstrating that a single resonator is capable of providing a useful signal at multiple frequencies. This is useful in terms of the production of a CSAC, since it simplifies the system architecture in cases, such as for field feedback, where multiple frequencies are required. Maximum simplicity is essential for effective microfabrication.

Whilst progress has been made in the development of using multiple frequencies simultaneously in order to enable field feedback, a stable proof of concept is yet to be realised. A number of routes to further progress are offered in section 4 above, but it is evident that making this work will not be straightforward and contains more technical difficulty than originally anticipated.

Considering the above successes in the wider scenario of building a successful and competitive CSAC, however, indicates that there is still a significant amount of work to be done in realising this, even in the simplest form of using the clock transition with a single frequency and a critically coupled resonator.

Whilst the estimated short term ADEV achieved here of $2.8 \times 10^{-4} \, \tau^{-\frac{1}{2}}$ is an improvement on past experiments, it is still far greater than the average of this figure of merit for currently available CSACs in Table 2, which is of order 10^{-10} for $\tau = 1$ s. An estimate of the long term ADEV for the proposed ^{15}N@C$_{60}$ system is not yet possible since work on the frequency stabilisation mechanism is still under way. However, the short term figure is a useful comparator, improvements in which are essential for the resultant clock to be competitive with existing devices.

In [54], Harding et al describe potential improvements to their similar spectrometer, including a quantitative route to $\sigma_y(\tau = 1 \text{ s}) \approx 10^{-10}$. These are specified in Table 6 below. The work undertaken on resonators in section 4.1 goes some way toward the $Q = 200$ figure in the Table, and the potential further improvements suggested should provide a further increase.

Although I used a sample with higher purity (22 000 ppm) than Harding et al, some of the original sample was lost in preparation. A spin density measurement at X-band was not possible during the course of this work, but sweeps using the spectrometer detailed above yielded a comparable signal to an existing sample of ~6 500 ppm. This is similar to the ~6000 ppm used by Harding et al, and hence a similar spin density (~n ≈ 2.5 × 10²² m⁻³). In 2022, Thwaites [70] demonstrated that a higher short term ADEV is possible using a spectrometer essentially the same as that used here, but with modified loop gap resonators, by using DPPH in powder form, which has a much higher spin density. Thwaites reports $\sigma_y(\tau = 1\ s) \approx (1.93 \pm 0.04) \times 10^{-5}$ using this setup.

These results demonstrate improvement in line with that suggested by Harding et al in an EPR-based system, indicating that the first three suggestions of Table 6 will be effective.

Limiting Factor	Change	Relative Improvement
Purity (%)	0.6 → 100	170
Concentration (mg/ml)	5 → 51	10
Resonator Q factor	70 → 200	2.9
Electronic noise (nV Hz$^{-1/2}$)	2.5 → 0.9	2.8
Linewidth (Hz)	$10^5 \rightarrow 10^2$	1000
	Product	1.4×10^7

Table 6. Potential improvements to a ^{15}N@C$_{60}$ based frequency standard in order to achieve $\sigma_y(\tau = 1\ s) \approx 10^{-10}$. Reproduced from [54].

The last two suggested improvements in Table 6 lie outside the scope of this thesis, however, as mentioned in section 4 above, significant electronic noise was observed during the measurements, the many causes of which included the simple shape and direction of placement of a coaxial cable. Since Rinard et al [71] have reported EPR spectrometer measurements with a $SNR \approx 1$, it is not unreasonable to speculate that the integration and microfabrication of the electronics physics package of the proposed CSAC could reduce some of this noise through shielding and the elimination of antenna behaviour within the circuitry. However, to be competitive with the SWaP of existing CSAC devices (see Table 2), it will be necessary for components and circuitry to be in close proximity, increasing the likelihood of factors such as parasitic capacitance and inductance. This reduces the likelihood of producing a $SNR \approx 0.9$, since this represents the Johnson-Nyquist thermal noise limit at room temperature with ideal system components.

Further considerations for noise mitigation would be necessary if considering a ^{15}N@C$_{60}$ based clock, due its frequency of operation and domain of useful operation in devices such as navigation equipment. Similar frequencies are used by radio based equipment, some of which are high amplitude, such as radio astronomy [72] and meteor burst communications [73], which use frequencies between 30 and 100 MHz in the high atmospheric domain, resulting in significant potential interference.

Similar considerations, though at higher frequencies, would apply to the proposal of Harding et al for a ^{31}P@C$_{60}$ clock, which has a clock transition at ~240 MHz. This endohedral fullerene retains the molecular advantages and solubility of ^{15}N@C$_{60}$ whilst providing a significant improvement in SNR and transition quality factor (due to their

frequency dependence), along with a narrower linewidth and weaker temperature dependence [54].

The qualities of ^{31}P@C_{60}, and the fact that the spectrometer and resonator improvements demonstrated in this thesis can be applied in the same way to this molecule, suggest that this should be the next step in the development of an endohedral fullerene based atomic frequency standard, and ultimately, a CSAC based on this technology. The improvement in ADEV from higher spin density demonstrated by Thwaites [70] further indicates that higher purity and concentrations will yield better results. Whilst the production of ^{31}P@C_{60} will require new methodologies, which will take some time to develop, higher sample spin densities of ^{15}N@C_{60} can be used in the meantime to experimentally quantify the ADEV improvement.

Work is currently underway, in the group of Prof Edward Laird at Lancaster University, to develop and demonstrate the frequency-swept configuration necessary for clock operation, and the frequency feedback mechanism described in section 3.5 above. The results of section 4.3 and 4.4 indicate that, subject to the resolution of circuitry problems, multiple frequency measurements with a single resonator are possible, enabling the possibility of a simultaneous field feedback mechanism which would further protect a clock from environmental field fluctuations.

These final considerations indicate that an endohedral fullerene based frequency standard in a CSAC form is a real possibility, but that ^{31}P@C_{60} would provide a better basis for a more competitive stability metric than ^{15}N@C_{60}. Whilst the best vapour-based CSACs may still yield a lower short term ADEV, the reduction in complexity of a radio frequency, EPR based standard will likely yield a better SWaP-C, potentially making it more suitable in some scenarios such as mass-production requiring low cost.

Outlook

The ultimate goal of the wider project of which this thesis forms a part is to create a microfabricated assembly which replicates the function of the EPR spectrometer and physics package detailed in the foregoing sections. It is envisaged that this will fit into a DIP (dual in-line package) microchip which may be fixed to a PCB (printed circuit board) either in a through-hole soldered format or via a socket layer. The three sets of coaxial coils will be positioned around a sample container inside the B_1 coil. The inductive coupling will be fixed and connected to an on-board filtering and signal processing unit, including feedback mechanisms for both frequency and field, and a one pulse per second output. The chip itself will be magnetically shielded and thermally stabilised.

Further experiments with different reference material containment configurations are required to determine the best way to store the sample. The liquid solution in CS_2 is convenient for the experiments here but limits the spin density to the saturation level of C_{60} in carbon disulfide. A powder sample would provide much higher spin density but may be more sensitive to Orbach processes which affect decoherence times and broaden the linewidth. Any potential dipolar coupling between Nitrogen atoms due to their increased proximity would also need to be quantified and accounted for in signal processing. Furthermore, an additional temperature dependence is introduced in the powder format, since below 249 K, C_{60} forms an orientationally ordered cubic lattice [74], which may in turn affect the two foregoing considerations.

Deposition of the endohedral fullerenes onto a substrate may also be possible and may be assembled in such a way as to serve to cushion the sample from acoustic or physical oscillations. However, care would need to be taken to ensure the signal was not affected by the substrate nor additional signals introduced.

It is envisaged that, given the relative simplicity of the components, such microfabrication will be possible, with the result being a competitive CSAC in situations where low SWaP-C is a priority.

Appendix 1 – Spectrometer Specification

The instruments and components used in the spectrometer are specified below. All elements not in the table were either produced in the laboratory or are generic parts.

Instruments	Manufacturer and Model no. / Specification
RF signal generator	RIGOL DSG821A
Waveform generator (modulation)	Keysight 33500B
Lock-in amplifier	Zurich Instruments MFLI
DC supply (Helmholtz coils)	Keithley 2280S-32-6
DC supply (amplifiers)	TENMA 72-10495
Vector network analyser	Copper Mountain S5048
Components	
Attenuator	Vaunix LDA
Directional coupler	Mini Circuits ZX30-12-4-S+
Band pass filters between directional coupler and mixer	Mini Circuits HPF / LPF with frequencies suitable for experimental case.
Amplifiers	Mini Circuits ZX60-3018G-S+
Mixer	Mini Circuits ZP-5MH-S+
Low pass filter between mixer and lock-in	Thor Labs EF122; 20 kHz LPF
Signal cables	SMA, 50 ohm
Power cables	BNC, 50 ohm

Table 7. Spectrometer specification.

Appendix 2 – Glossary of Terms

E_{67}	The energy difference between energy eigenvalues 6 and 7
$\boldsymbol{B}_0$	The static (swept) magnetic field in the EPR spectrometer
$\boldsymbol{B}_1$	The oscillating drive field in the spectrometer
$\boldsymbol{B}_{mod}$	The modulation field in the spectrometer
$\lvert A \rvert / h$	The modulus of the hyperfine constant divided by Planck's constant (gives a frequency)
^{15}N@C$_{60}$	Nitrogen-15 in Carbon-60; an endohedral fullerene
^{31}P@C$_{60}$	Phosphorous-31 in Carbon-60; an endohedral fullerene
ADEV, $\sigma_y(\tau)$	Allan deviation
AVAR	Allan variance
C$_{60}$	Carbon-60 or Buckminster Fullerene
CAD	Computer aided design
CBT	Caesium Beam Tube
CPT	Coherent population trapping
CS$_2$	Carbon disulfide
CSAC	Chip scale atomic clock
CW EPR	Continuous wave electron paramagnetic resonance
DPPH	2,2-diphenyl-1-picrylhydrazyl
EPR	Electron paramagnetic resonance
FWHM	The full width at half maximum
GLONASS	Global'naya Navigatsionnaya Sputnikovaya Sistema (the Russian GNSS)
GNSS	Global Navigation Satellite Systems
GPS	Global Positioning System
H maser	Hydrogen Maser
HPLC	High pressure liquid chromatography
IMD	Intermodulation distortion
LC	Inductor-capacitor
LGR	Loop gap resonator
Linewidth	The width of the spectral line produced by a measured resonance
LLC	Inductor-inductor-capacitor
LO	Local oscillator
LTC	Lunar Coordinated Time
MDEV	Modified Allan Deviation
MDS	Multi device synchronization (a Zurich instruments protocol)
MEMS	Micro-electromechanical system
MLGR	Modified loop gap resonator
MODR	Microwave optical double resonance
NIST	National Institute of Standards and Technology (in the USA)
NPL	National Physical Laboratory
RF	Radio frequency
RLC	Resistor-inductor-capacitor
SNR	Signal to noise ratio
SWaP	Size, Weight and Power
SWaP-C	Size, Weight, Power and Cost
TAI	International Atomic Time
TDEV	Time deviation

UTC	Coordinated Universal Time
VCSEL	Vertical-cavity surface-emitting laser
VNA	Vector network analyser

Bibliography

1. Panfilo G, Arias F. The Coordinated Universal Time (UTC). Vol. 56, Metrologia. Institute of Physics Publishing; 2019.
2. Lombardi MA, Novick AN, Neville-Neil G, Cooke B. Accurate, traceable, and verifiable time synchronization for world financial markets. Journal of Research of the National Institute of Standards and Technology. 2016;121:436–63.
3. Kouba J. Relativistic Time Transformations in GPS [Internet]. Vol. 5, GPS Solutions. 2002. Available from: http://igscb.jpl.nasa.gov
4. Agnew DC. A global timekeeping problem postponed by global warming. Nature [Internet]. 2024 Mar 27; Available from: https://www.nature.com/articles/s41586-024-07170-0
5. Schechner S. The Material Culture of Astronomy in Daily Life: Sundials, Science, and Social Change. Journal for the History of Astronomy. 2001; 32: 189-222.
6. Margolis H. A Brief History of Timekeeping. Vol. 31, Phys. World. 2018.
7. Blumenthal AS, Nosonovsky M. Friction and Dynamics of Verge and Foliot: How the Invention of the Pendulum Made Clocks Much More Accurate. Applied Mechanics. 2020 Jun 1;1(2):111–22.
8. The Open University. Physics: from Classical to Quantum. Vol. 1. Milton Keynes. The Open University Press; 2017.
9. Katzir S. Pursuing frequency standards and control: The invention of quartz clock technologies. Vol. 73, Annals of Science. Taylor and Francis Ltd.; 2016. p. 1–39.
10. Nizhnik O, Higuchi K, Maenaka K. Quartz resonator based, 0.12 μW, 32768 Hz oscillator with ±100 ppm frequency accuracy. Journal of Low Power Electronics and Applications. 2011 Sep 20;1(2):327–33.
11. Porfyrakis K, Laird EA. Keeping Perfect Time With Caged Atoms. Vol. 54, IEEE Spectrum 2017. p. 34-39
12. Lombardi MA. A Historical Review of U.S. Contributions to the Atomic Redefinition of the SI Second in 1967. Vol. 122, Journal of Research of the National Institute of Standards and Technology. National Institute of Standards and Technology; 2017.
13. Newell DB, Tiesinga E. The international system of units (SI): [Internet]. Gaithersburg, MD; 2019 Aug. Available from: https://nvlpubs.nist.gov/nistpubs/SpecialPublications/NIST.SP.330-2019.pdf
14. Sébastien Bize. The unit of time: Present and future directions. Comptes Rendus. Physique, Volume 20 (2019) no. 1-2, pp. 153-168
15. Oxford University Press. Oxford Reference; Proper Time [Internet]. 2024. Available from: https://www.oxfordreference.com/display/10.1093/oi/authority.20110803100349685
16. McCarthy DD. The Definition of UTC. International Astronomical Union Colloquium. 2000 Mar;180:363–71.
17. Dimarcq N, Gertsvolf M, Mileti G, Bize S, Oates CW, Peik E, et al. Roadmap towards the redefinition of the second. Vol. 61, Metrologia. Institute of Physics; 2024.
18. Li R, Gibble K, Szymaniec K. Improved accuracy of the NPL-CsF2 primary frequency standard: Evaluation of distributed cavity phase and microwave lensing frequency shifts. Metrologia. 2011;48(5):283–9.

19. Bauch A. Caesium atomic clocks: function, performance and applications. Vol. 14, Measurement Science and Technology. 2003. pp. 1159-1173.
20. Heavner TP, Donley EA, Levi F, Costanzo G, Parker TE, Shirley JH, et al. First accuracy evaluation of NIST-F2. Metrologia. 2014;51(3):174–82.
21. Marlow BLS, Scherer DR. A review of commercial and emerging atomic frequency standards. IEEE Transactions on Ultrasonics, Ferroelectrics, and Frequency Control. 2021 Jun 1;68(6):2007–22.
22. Hellwig HW. Atomic frequency standards: A survey. Vol 63, Proc. IEEE, pp. 212–229. 1975.
23. Mattioni L, Belloni M, Berthoud P, Pavlenko I, Schweda H, Wang Q, Rochat P et al. The Development of a Passive Hydrogen Maser Clock for the Galileo Navigation System. Proceedings of the 34th Annual Precise Time and Time Interval Systems and Applications Meeting, Reston, Virginia, pp. 161-170. 2002.
24. Godone A, Levi F, Calosso CE, Micalizio S. High-performing vapor-cell frequency standards. Rivista del Nuovo Cimento. 2015 Mar 1;38(3):133–71.
25. Katori H, Takamoto M, Pal'chikov VG, Ovsiannikov VD. Ultrastable Optical Clock with Neutral Atoms in an Engineered Light Shift Trap. Phys. Rev. Lett. 91, 173005. 2003.
26. Bloom BJ, Nicholson TL, Williams JR, Campbell SL, Bishof M, Zhang X, et al. An Optical Lattice Clock with Accuracy and Stability at the 10^{-18} Level. Nature, vol. 506, p. 71, Jan. 2014
27. Hannig S, Pelzer L, Scharnhorst N, Kramer J, Stepanova M, Xu ZT, et al. Towards a transportable aluminium ion quantum logic optical clock. Review of Scientific Instruments. 2019 May 1;90(5).
28. Ludlow AD, Boyd MM, Ye J, Peik E, Schmidt PO. Optical atomic clocks. Reviews of Modern Physics. 2015 Jun 26;87(2).
29. Gouloumet J, Leuenberger B, Schori C, Grop S, Rochat P. Progress towards a compact and low-power miniaturized Rubidium Oscillator (mRO™). IEEE/MTT-S International Microwave Symposium (IMS). IEEE; 2020.
30. Kitching J. Chip-scale atomic devices. Vol. 5, Applied Physics Reviews. American Institute of Physics Inc.; 2018.
31. Vanier J. Atomic clocks based on coherent population trapping: A review. Vol. 81, Applied Physics B: Lasers and Optics. 2005. p. 421–42.
32. IEEE standard definitions of physical quantities for fundamental frequency and time metrology - random instabilities. Standard 1139-2022. 2022.
33. Riley W.NIST special publication 1065: Handbook of Frequency Stability Analysis. Gaithersburg, MD, USA. NIST; 2008.
34. Techspot.com [internet]. The Caesium 133 is the world's first true atomic wristwatch. Available from: https://www.techspot.com/news/56372-the-cesium-133-is-the-worlds-first-true-atomic-wristwatch.html
35. Shin DH, Sung TK. Comparisons of error characteristics between TOA and TDOA positioning. IEEE Transactions on Aerospace and Electronic Systems, 38:307–311. 2002.
36. Travagnin M. Chip-Scale Atomic Clocks Physics, technologies, and applications. European Commission Joint Research Centre. Luxembourg. 2021.
37. British Broadcasting Corporation. BBC News [internet]. White House wants Moon to have its own Time Zone. Available from: White House wants Moon to have its own time zone - BBC News

38. Lee SW, Kim J, Jeong MS, Lee YJ. Monitoring atomic clocks on board GNSS satellites. Advances in Space Research. 2011 May 17;47(10):1654–63.

39. Hauser E. UNIX time, UTC, and datetime: Jussivity, prolepsis, and incorrigibility in modern timekeeping. Proceedings of the Association for Information Science and Technology. 2018 Jan 1;55(1):161–70.

40. McDowell JC. The Low Earth Orbit Satellite Population and Impacts of the SpaceX Starlink Constellation. The Astrophysical Journal Letters. 2020 Apr 1;892(2):L36.

41. Tazaki R, Lazarian A, Nomura H, Rekveldt MT, Keller T, Golub R. Larmor precession, a technique for high-sensitivity neutron diffraction. Vol. 54, Europhys. Lett. 2001; pp342-346.

42. Slichter CP. Principles of Magnetic Resonance. Springer-Verlag, 2nd, Revised and Expanded Edition. 1978.

43. Smith TD, Pilbrow JR. The determination of structural properties of dimeric transition metal ion complexes from epr spectra. Vol 13, Coordination Chemistry Reviews 2–3.1974. pp173-278.

44. Lockyer SJ, Nawaz S, Brookfield A, Fielding AJ, Vitorica-Yrezabal IJ, Timco GA, et al. Conformational Flexibility of Hybrid [3]- A nd [4]-Rotaxanes. Journal of the American Chemical Society. 2020 Sep 16;142(37):15941–9.

45. Bock CH, van der Est AJ, Brettel K, Stehlik D. Nanosecond electron transfer kinetics in photosystem I as obtained from transient EPR at room temperature. Vol. 247. 1989.

46. Little E, Mrozek J, Rogers C, Liu J, Mcinnes E, Bowen A et al. Experimental Realisation of Multi-Qubit Gates Using Electron Paramagnetic Resonance. Nature Communications. 2023 Sept 28.

47. Zavoisky E. Spin-magnetic resonance in paramagnetics. J. Phys. (USSR). 9: 245. 1945.

48. Rinard GA, Eaton GR. Loop-Gap Resonators. Department of Engineering and Department of Chemistry and Biochemistry, University of Denver. Denver, Colorado. University of Denver; 2005.

49. Harding R. Endohedral fullerenes as standards for portable atomic clocks [thesis]. Oxford, UK. Oxford University. 2019.

50. Indica DJ. Fine hyperfine levels.png. Creative Commons, Wikimedia [internet]. Accessed 2024. Available from: File:Fine hyperfine levels.png - Wikimedia Commons

51. Lowe DJ. ENDOR and EPR of Metalloproteins. Vol. 57, Biophys. M&M. Biol. 1992.

52. Bertran A, De Zotti M, Timmel CR, Di Valentin M, Bowen A. Determining and controlling conformational information from orientationally selective Light-Induced Triplet–Triplet Electron Resonance spectroscopy for a set of bis-porphyrin rulers. Physical Chemistry Chemical Physics. 2023 Oct 31.

53. GyroMagician. Nmr fid good shim.svg. Reproduced using Creative Commons license https://creativecommons.org/licenses/by-sa/3.0. Available from: Nmr fid good shim EN - Free induction decay - Wikipedia

54. Harding RT, Zhou S, Zhou J, Lindvall T, Myers WK, Ardavan A, et al. Spin Resonance Clock Transition of the Endohedral Fullerene N 15 @ C60. Physical Review Letters. 2017 Oct 4;119(14).

55. Green M. Fit Derivation and Lock-In [unpublished]. Lancaster University. 2023.

56. Henderson S. LocatorX Internship - Construction, Modelling and Improvement of Tabletop Atomic Clock Designs [unpublished]. Lancaster University. 2023.

57. Murphy TA, Pawlik T, Weidinger A, Höhne M, Alcala R, Spaeth JM. Observation of Atomlike Nitrogen in Nitrogen-Implanted Solid C 60. 1996.

58. Pietzak B, Waiblinger M, Almeida Murphy T, Weidinger A, Hahne M, Dietel E, et al. PROPERTIES OF ENDOHEDRAL $N@C_{60}$. Vol. 36, Carbon. 1998.

59. Harneit W, Meyer C, Weidinger A, Suter D, Twamley J. Architectures for a spin quantum computer based on endohedral fullerenes. In: Physica Status Solidi (B) Basic Research. 2002. p. 453–61.

60. Benjah-bmm27. Buckminsterfullerene-perspective-3D-balls.png [internet]. Wikimedia Commons. Accessed 2024. Available from: Buckminsterfullerene-perspective-3D-balls - Buckminsterfullerene - Wikipedia

61. Lindvall T. MAC Theory Report - $^{15}N@C_{60}$ atomic system [unpublished]. VTT Technical Research Centre of Finland. 2015 Dec 17.

62. Karlen S, Gobet J, Overstolz T, Haesler J, Lecomte S. Lifetime assessment of RbN_3-filled MEMS atomic vapor cells with Al_2O_3 coating. Optics Express. 2017 Feb 6;25(3):2187.

63. Morton JJL, Tyryshkin AM, Ardavan A, Porfyrakis K, Lyon SA, Andrew G, et al. Electron spin relaxation of N@C 60 in CS 2. 2006.

64. Vigneau F, Fedele F, Chatterjee A, Reilly D, Kuemmeth F, Gonzalez-Zalba MF, et al. Probing quantum devices with radio-frequency reflectometry. Vol. 10, Applied Physics Reviews. American Institute of Physics Inc.; 2023.

65. Eaton GR, Eaton SS, Barr DP, Weber RT. Quantitative EPR. New York. Springer Wien. 2010.

66. Kalendra V, Turčak J, Banys J, Morton JJL, Šimėnas M. X- and Q-band EPR with cryogenic amplifiers independent of sample temperature. Journal of Magnetic Resonance. 2023 Jan 1;346.

67. Maas, A. How to Model Intermodulation Distortion. Dept. of Electrical Engineering, University of California Los Angeles. 1991.

68. Meyer RG, Shensa MJ, Eschenbach R. Cross Modulation and Intermodulation in Amplifiers at High Frequencies. IEEE Journal of Solid-State Circuits, vol. SC-7, no. 1, Feb 1972.

69. Tian S, Lee FC, Li Q. Equivalent Circuit Modeling of LLC Resonant Converter. IEEE Transactions on Power Electronics. 2020 Aug 1;35(8):8833–45.

70. Thwaites RJ. Electron Paramagnetic Resonance Spectroscopy for Atomic Clock Applications [thesis]. Lancaster University. 2022.

71. Rinard GA, Quine RW, Song R, Eaton GR, Eaton SS. Absolute EPR Spin Echo and Noise Intensities. 1999; Journal of Magnetic Resonance 140, 69–83.

72. Ofcom. United Kingdom Frequency Allocation Table. 2017. Issue no. 18 v1.1. Available from: http://static.ofcom.org.uk/static/spectrum/fat.html.

73. Craig Cumberland BB, Valacich JS, Jessup LM. Understanding Meteor Burst Communications Technologies. Vol. 47, P. SPURNY. 2004.

74. David WIF, Lbberson RM, Matthewman JC, Prassides K, John T, Dennis S, et al. Crystal structure and bonding of ordered c60. 1991.